

AD _____

Award Number: DAMD17-99-1-9379

TITLE: Improving Detection of Axillary Lymph Nodes by Computer-Aided Kinetic Feature Identification in Positron Emission Tomography

PRINCIPAL INVESTIGATOR: Xiaoli Yu, Ph.D.

CONTRACTING ORGANIZATION: University of Southern California
Los Angeles, California 90023

REPORT DATE: August 2001

TYPE OF REPORT: Annual

PREPARED FOR: U.S. Army Medical Research and Materiel Command
Fort Detrick, Maryland 21702-5012

DISTRIBUTION STATEMENT: Approved for Public Release;
Distribution Unlimited

The views, opinions and/or findings contained in this report are those of the author(s) and should not be construed as an official Department of the Army position, policy or decision unless so designated by other documentation.

20020719 097

REPORT DOCUMENTATION PAGE			Form Approved OMB No. 074-0188	
<small>Public reporting burden for this collection of information is estimated to average 1 hour per response, including the time for reviewing instructions, searching existing data sources, gathering and maintaining the data needed, and completing and reviewing this collection of information. Send comments regarding this burden estimate or any other aspect of this collection of information, including suggestions for reducing this burden to Washington Headquarters Services, Directorate for Information Operations and Reports, 1215 Jefferson Davis Highway, Suite 1204, Arlington, VA 22202-4302, and to the Office of Management and Budget, Paperwork Reduction Project (0704-0188), Washington, DC 20503</small>				
1. AGENCY USE ONLY (Leave blank)		2. REPORT DATE August 2001		3. REPORT TYPE AND DATES COVERED Annual (1 Aug 00 - 31 Jul 01)
4. TITLE AND SUBTITLE Improving Detection of Axillary Lymph Nodes by Computer-Aided Kinetic Feature Identification in Positron Emission Tomography			5. FUNDING NUMBERS DAMD17-99-1-9379	
6. AUTHOR(S) Xiaoli Yu, Ph.D.				
7. PERFORMING ORGANIZATION NAME(S) AND ADDRESS(ES) University of Southern California Los Angeles, California 90023 E-Mail: <u>xiyu@milly.usc.edu</u>			8. PERFORMING ORGANIZATION REPORT NUMBER	
9. SPONSORING / MONITORING AGENCY NAME(S) AND ADDRESS(ES) U.S. Army Medical Research and Materiel Command Fort Detrick, Maryland 21702-5012			10. SPONSORING / MONITORING AGENCY REPORT NUMBER	
11. SUPPLEMENTARY NOTES Report contains color				
12a. DISTRIBUTION / AVAILABILITY STATEMENT Approved for Public Release; Distribution Unlimited				12b. DISTRIBUTION CODE
13. ABSTRACT (Maximum 200 Words) The goal of this project is to improve detection of metastatic axillary breast cancer through sophisticated physiological modeling and statistical signal processing techniques. The major focus of Year 2 was to develop statistical hypothesis test criteria for the computer-aided detection of kinetic features in metastases, which was built on modeling, extracting and exploiting physiological features pursued since the last reporting period. Three types of generalized likelihood ratio tests (GLRT) were derived under different assumptions on pixel spatial correlation. We compared these three GLRTs using three different methods of TAC evaluation and computer generated phantom data. The lesions in the phantom data were fully invisible. The results show that the best of the three achieved 97, 79% and 88% for specificity, sensitivity and accuracy, respectively. Further work on validation and evaluation of physiological feature modeling, kinetic parameter estimation and objective rank-reduction of dynamic PET sinogram for fast image reconstruction has also been continued through this year. The results of the initial clinical dataset studied are promising, but too small to make a conclusive decision. The assessment of all findings in theory and simulations in Year 1 and Year 2 will be continued in the Year 3 when more clinical data will be available.				
14. SUBJECT TERMS Breast Cancer, axillary disease, PET, statistical signal processing			15. NUMBER OF PAGES 101	
			16. PRICE CODE	
17. SECURITY CLASSIFICATION OF REPORT Unclassified	18. SECURITY CLASSIFICATION OF THIS PAGE Unclassified	19. SECURITY CLASSIFICATION OF ABSTRACT Unclassified	20. LIMITATION OF ABSTRACT Unlimited	

Table of Contents

Cover.....	1
SF 298.....	2
Table of Contents.....	3
Introduction.....	4
Body.....	4
Key Research Accomplishments.....	7
Reportable Outcomes.....	8
Conclusions.....	9
References.....	9
Appendices.....	11

1. Introduction

Intensive efforts are underway to develop small PET systems dedicated to functional imaging of breast cancer. These system developments will still require sophisticated analyses of dynamic PET images to detect small lesions. We have been seeking a clinically practical way to assist conventional visual inspection of static PET images with temporal information derived from a dynamic PET-FDG imaging sequence. Modeling, extracting and exploiting physiological features that can distinguish normal breast tissues from axillary malignancies in dynamic PET has been pursued since the last reporting period. The study conducted in the current year was built on the previous year's research, which concentrated on the development and testing of optimal computer-aided detection criteria for kinetic feature identification from equivocal axillary metastases in noisy images. Rather than replace conventional visual image inspection, our goal is to design an intelligent system that will supplement it.

The whole proposed study consists of four tasks: **Task 1:** Developing the mathematical formula to linearly map and identify the physiological features contained in PET dynamic sinogram sequence (*Month 1-8*), **Task 2:** Developing the schemes for objective reduction of dynamic sinogram data guided by the identified TAC subspaces of the desired signal (tumor) and the interference (normal tissue background plus noise) (*Month 4 - 12*), **Task 3:** Deriving and analyzing statistical hypothesis test criteria to test the presence of an axillary metastasis in the dynamic images reconstructed from the compressed sinogram data (*Month 13 - 24*), and **Task 4:** Clinical Evaluation (*Month 13 - 36*). For each task, several subtasks were defined (see the SOW in the grant application for details).

2. Body

During this annual reporting period, our efforts were mainly focused on Tasks 3 and 4. These two tasks were those originally proposed for the second year of the study. After last year's annual report, it was brought to our attention that we needed to obtain approval from the U.S. Army Medical Research and Materiel Command Institutional Review Board (US Army IRB). Although patients whose data are used in this study will have a PET scan regardless of their participation in this study, they still must be prospectively recruited for "additional" (temporal-based) images. Efforts have been underway for the last 6 to 8 months to complete the respective IRB approvals with protocol/language acceptable to USC's Institutional Review Board and the US Army IRB. Because IRB approval is pending, no dynamic imaging data have been acquired nor any subjects recruited for the extra pictures since that time. Efforts in support of Task 4 have been limited to analyses of dynamic imaging data that already existed in the patient database of USC PET center. Further work on Tasks 1 and 2 has also been continued through this year. The major accomplishments of this activity are presented as follows. The technical details and related results can be found in Appendices.

2.1 Evaluation and Validation of PET-FDG tracer kinetic models and subspace representations (*Task 1 continuation*).

Last year utilizing a literature search, we reviewed various types of mathematical models of PET-FDG kinetics. We selected the three-compartmental (or 4-K compartmental model) to use in these analyses [1].

Evaluation and validation of the standard PET-FDG 3-compartment metabolic models in homogeneous and heterogeneous tissues was performed on dynamic PET data from the image database at the USC PET center. Among them, 7 breast cancer and 5 lung cancer cases were used for the kinetic analysis. In these images there were 7 primary breast tumors, 2 axillary metastases, 5 primary lung tumors as well as 2 lung metastases. All were proven by pathology.

Using the clinical data, the hypothesis that the kinetic features of primary tumors and metastases are similar but they are different in malignant and normal tissues was tested. For each patient data, ROIs were selected in well-defined primary tumor, metastases and normal tissues, respectively. In the ROIs, we observed that the radiotracer uptake within the primary tumors or metastases increases with time, while the TAC decreases for normal tissues. To further reveal the similarities and differences in kinetic parameters, two methods were employed to fit the time activity curves measured in different tissue types with the three compartmental kinetic models. The first assumed homogeneity within the ROIs and the other method accounted for potential heterogeneity. In the homogeneous PET-FDG modeling, the nonlinear parameter estimation with the Newton-Raphson algorithm was used to estimate the rates of transport of FDG in plasma to tissue, K_1 , k_2 , k_3 , and k_4 , while fitting the time activity curves. The corresponding macro-parameters, which define the physiological factors uniquely associated to tissue types, were computed from the estimations of k 's. In heterogeneous tissue, the time activity curve generated by the ROI represents the mass-weighted average concentration of radioactivity in several different "homogeneous" tissues. Thus, the physiological factors demonstrated in heterogeneous tissues really represent those from several homogeneous tissues [1,2]. The multidimensional maximum likelihood estimation (MLE) method [7,8] was utilized to estimate the macro-parameters of physiological factors in heterogeneous tissues. We found that no significant "distance" between macro-parameter clusters of primary and metastases. But the "distance" of macro-parameter clusters between malignancy and normal tissue was significantly different (> 0.006 and 0.001) for breast and lung cancers, respectively. We also found that the use of heterogeneous model and the MLE results in improved lesion detectability, specifically with respect to false positive and false negative findings, although the mean square errors generated by fitting the time activity curve were about the same for the two models. Since the initial dataset studied is too small to make a conclusive decision, the assessment of the two models and their associated kinetic parameter estimations will be continued in the third year when more clinical data will be available.

2.2 Identification of Physiological subspace directly from PET projection data *(Continuation for Task 2)*

A data processing scheme was developed to directly identify the kinetic parameters and the corresponding subspace features of the lesions. Instead of reconstructing all frames of

dynamic images for kinetic analysis, our method selectively reconstructs only one frame. This frame is most often the one with the longest acquisition time period or highest signal-to-noise ratio. From the selected image, the ROIs can be defined, which provides in turn the ROIs for the sinogram domain. Different than the image data, each observation in sinogram contains contributions from all image pixels on a ray line. Thus, filtering has to be performed in order to remove the superimposed contributions from other pixels before proceeding to estimation of subspace parameters in the sinogram ROIs. The filtered data provide a more accurate parameter estimation. A filter was designed which turned out to be a local filtered backprojection operator. The implementation of the filter in C++ was completed.

2.3 Performance test of data compression algorithms for fast dynamic PET image reconstruction *(Task 2 continuation)*

Three rank-reduction criteria that lower the dimensionality of dynamic sinogram in time domain and speed up dynamic image reconstruction, developed in the first year, were further evaluated with computer generated phantom dynamic data. The time activity curves of the primary, metastatic lesions and normal tissues in the phantom data were true clinical observations. A ROC study on the phantom data is ongoing to assess these three algorithms in terms of lesion detectability (false positive and false negative rates). To date, our results show the proposed maximum SNR criterion outperforms the conventional SVD and maximum signal energy methods in terms of enhancing lesion to background contrast in reconstructed images. This is because that the maximum SNR method best maintains the characteristics of the lesion time activity curve after compression, while both the SVD and the maximum signal energy methods [3, 9] change the characteristics of time activity curve in the lesion substantially.

The performance assessment of the compression algorithm with clinical data will continue to be pursued in the third year. The data processing scheme and the related software, described in section 2.2, is to be applied to estimate kinetic features directly from PET sinogram. The estimated features will be used in the developed maximum SNR criterion of data compression.

2.4 Development of statistical hypothesis test criteria for the computer-aided metastasis detection *(Task 3)*

Using the subspace kinetic features identified from well-defined malignancies for computer-aided detection of non-palpable metastases was accomplished by the development of statistical hypothesis test criteria and decision rules. These criteria are aimed at distinguishing the subspace features intrinsic to both malignancy and normal tissues.

The generalized likelihood ratio test (GLRT) is a standard procedure for solving statistical detection problems [5]. During this year, three types of GLRTs were derived for the different assumptions on pixel spatial correlation. The first GLRT, that is an extension of the algorithm first developed in [5], assumes that pixels in an arbitrarily selected ROI are

spatially uncorrelated. Two different hypothesized data models were used to characterize the observations of large lesions and small lesions. In practice, image pixel values are not statistically uncorrelated because each count contributes to all pixel values when an image is reconstructed, so the second GLRT adds a pre-whitening procedure to the first. The spatial covariance matrix required for the pre-whitening process is to be computed using the methods given in [4,6]. Finally, the third GLRT extended the first by assuming that the spatial inter-pixel correlation in each frame has the same structure but different energy level.

The technical details in sections 2.1 – 2.4 can be found in Dr. C.C. Huang's thesis, which is attached to this report as Appendix A.

2.5 Comparison and evaluation of three developed hypothesis test criteria (Tasks 3 and 4)

We compared three developed detection criteria using three different methods of TAC evaluation by computer generated phantom data. The first method studied was conventional averaging over an ROI, which assumes no spatial correlation between pixels. The second method takes the spatial inter-pixel correlation into account. The covariance matrix is computed frame by frame, based on Huesman's analytical formulas and Carson's simplifications. In this method, the TACs for individual pixels in an ROI are first spatially decorrelated by the covariance matrix, and then averaged for kinetic parameter estimation. The third method assumes that the spatial inter-pixel correlation in the i -th frame has the form $\sigma_i R$, i.e., each frame has the same spatial correlation structure R , but a different energy level σ_i . Thus, the covariance matrix computed in the least noisy frames can be used as matrix R for noisier frames. For receiver-operator curve (ROC) study, the kinetic features estimated from these three methods are incorporated into the three GLRTs for lesion identification, developed from the generalized likelihood ratio principle as described above. The rates of true and false positives are counted to form ROC curves. We used 50 sets of dynamic phantom simulations with/without artificially inserted lesions. These lesions were assigned clinically measured TACs of malignant lung and breast tissues, respectively. The results show that Method 3 increased specificity and accuracy by 20 and 11%, respectively, as compared to the other two methods. No significant difference was observed between Methods 1 and 2, which could be due to inaccurate covariance matrix estimation introduced by the simplification made in the early frames. Further study of this will continue through the next year.

This work has been presented in SNM annual conference 2001, Toronto, Ca., June 2001, see Appendix D for details.

3. Key Research Accomplishments

The main accomplishments in Year 2 are

1. Evaluation of PET-FDG three compartmental models in homogeneous and heterogeneous tissues using clinical breast and lung cancer patient data, validation of the subspace representations for time activity curves (TAC) in different tissues,

such as primary tumors, metastases and normal tissues, etc. and quantification of the different kinetics between normal and malignant tissues as well as the similar kinetics between primary and metastatic lesion kinetics.

2. Establishment of a data processing scheme to estimate kinetic features of three compartmental models directly from PET sinogram and implementation of the scheme with C++.
3. Design of a filter to remove the contributions of unwanted image pixels from sinogram data for more accurate estimation of kinetic features from PET project data, test of filter performance in sinogram data and extension of the image-pixel-based estimation algorithms to a scan-projection-based approach.
4. Assessment of three data compression algorithms, developed in the last reporting period, for fast dynamic image reconstruction using computer generated phantom data. Comparison of the receiver-operating characteristic (ROC) curves between the original and compressed FBP dynamic images.
5. Development of statistical hypothesis test criteria for the computer-aided metastasis detection. Derivation of three statistical hypothesis test criteria by generalized maximum likelihood ratio principle that are able to distinguish the physiological factors (i.e. subspace features) associated to malignances and normal tissues.
6. Assessment of the three different hypothesis test criteria by performing a receiver operating characteristic (ROC) study on computer simulated phantom and small size of clinical data.
7. Accomplishment of the respective IRB approvals with protocol/language acceptable to USC's Institutional Review Board and the US Army IRB.

4. List of Reportable Outcomes:

4.1 Publications

1. C. C. Huang, "Computer-Aided Lesion Detection in Positron Emission Tomography: A Signal Subspace Fitting Approach", Ph. D. Thesis, submitted to Electrical Engineering Department of USC, May 2001.
2. X. Yu, C. C. Huang and P. S. Conti, "Assessment of ROI-based Time Activity Analyses in Dynamic PET For Oncology " *SNM Annual Conference 2001*, Toronto, Ca., June 2001.
3. X. Yu, C. C. Huang and R. Leahy, "Applied Subspace Identification, Filtering and Identification to Lesion Detection in Dynamic PET Images", revising for a submission to *IEEE Trans. on Medical Imaging*, December 2001.

4.2 Graduation

Two students graduated with their Ph. D. and M.S. degrees, respectively. Both were partially supported by this award.

5. Conclusion

In Year 2, study of physiological feature modeling, tumor identification and objective rank-reduction of dynamic PET sinogram for fast image reconstruction was continued. The mathematical models and algorithms developed in Year 1 were validated and evaluated with both computer generated phantom and a few sets of clinical data selected from the patient database of USC PET center. We found that there were no significant differences between macro-parameters of primary and metastatic tissue, which implies there are certain kinetic similarities between them. In contrast, a large difference was noted between malignant and normal tissue macro-parameters for both breast and lung cancers.

The major focus of Year 2 was to develop statistical hypothesis test criteria for the computer-aided detection of kinetic features in metastases. Three types of generalized likelihood ratio tests (GLRT) were derived under different assumptions on pixel spatial correlation. We compared these three GLRTs using three different methods of TAC evaluation and computer generated phantom data. The lesions in the phantom data were equivocal or invisible and assigned to time activity curves of malignant lung and breast tissues clinically measured in patient data. The results show that the best of the three increased specificity and accuracy by 20% and 11%, respectively, compared to the other two methods.

Results of Year 1 and Year 2 study indicate that it is potential to improve lesion detectability through sophisticated physiological modeling and statistical signal processing techniques. All findings in theory and simulations will be further tested and evaluated by a larger group of clinical patient data with proven primary breast cancer and palpable axillary metastases in Year 3.

6. References

1. K. Schmidt, G. Mies, and L. Sokoloff, "Model of kinetic behavior deoxyglucose in heterogeneous tissues in brain: A reinterpretation of the significant of parameters fitted to homogeneous tissue models," *J. Cerebral Blood Flow and Metabolism*, Vol. 11, p. 10-24, 1991.
2. F. Osullivan, "Imaging radiotracer model parameters in PET: A mixture analysis approach", *IEEE Trans. on Medical Imaging*, Vol. 12, No. 3, pp. 399-412, 1993.

3. C. M. Kao, J. T. Yap, J. Mukherjee and M. N. Wernick, "Image Reconstruction for Dynamic PET Based on Low-Order Approximation and Restoration of the Sinogram," *IEEE Trans. Medical Imaging*, Vol. 16, No. 6, Dec. 1997.
4. R. E. Carson, *et al.*, "An approximation formula for the variance of PET region-of-interest values," *IEEE Trans. Med. Imag.*, Vol. 12, No. 2, p. 240-250, June 1993.
5. L.L. Scharf and B. Friedlander, "Matched subspace detectors", *IEEE Trans. Signal Processing*, Vol. 42, No. 8, p. 2146-2157, Aug. 1994.
6. R.H. Huesman, "A new fast algorithm for the evaluation of regions of interest and statistical uncertainty in computed tomography," *Phys. Med. Biol.*, Vol. 29, No 5, p. 543-552, 1984.
7. C. C. Huang, X. Yu, J. Bading and P. S. Conti, "Feature extraction by subspace fitting of time activity curves in PET dynamic studies", *IEEE Medical Imaging Conference*, November 1997.
8. C.C. Huang, Ph.D. Thesis, submitted to USC EE department, May 2001.
9. P. Thanyasrisung, Ph.D. Thesis, submitted to USC EE department, May 2001.

Appendix A: Chapters of Dr. C. C. Huang's Ph.D. Thesis

Chapter 4

Dynamic Data Formulation and Subspace Identification

4.1 Overview

In computer-aided lesion detection with FDG-PET dynamic images, the TACs defined in Chapter 3 are useful for separating lesions from normal tissues [29]. However, how to identify the exponential subspace functions and incorporate the identified subspaces into a detector remains a problem. In this chapter, based on the dynamic temporal-spatial data structure, signal-subspace-fitting methods, such as the least squares (LS) method and the singular value decomposition (SVD) method, are used to estimate parametric (exponential function) and nonparametric (physiological factor) subspaces, respectively.

4.2 Dynamic Data Formulation

One of the advantages in the FDG-PET dynamic study is that the dynamic images can be formed into a temporal-spatial data matrix such that some useful signal array processing techniques can be applied. Let \mathbf{y}_k be the kinetic data measured by the PET scanner for the p -th pixel in a heterogeneous ROI, then

$$\begin{aligned}\mathbf{y}_k &= \mathbf{x}_k + \mathbf{n}_k \\ &= \mathbf{E}\mathbf{a}_k + \mathbf{n}_k\end{aligned}\tag{4.1}$$

where \mathbf{n}_p denotes the noise and is assumed to be Gaussian. Given that P denotes the number of pixels in the ROI, the temporal-spatial data matrix for the ROI from a PET scanner can be expressed as

$$\begin{aligned}\mathbf{Y} &\triangleq [\mathbf{x}_1, \mathbf{x}_2, \dots, \mathbf{x}_P] + [\mathbf{n}_1, \mathbf{n}_2, \dots, \mathbf{n}_P] \\ &= \mathbf{E}\mathbf{A} + \mathbf{N}\end{aligned}\tag{4.2}$$

where

$$\begin{aligned}\mathbf{A} &\triangleq [\mathbf{a}_1, \mathbf{a}_2, \dots, \mathbf{a}_P] \\ \mathbf{N} &\triangleq [\mathbf{n}_1, \mathbf{n}_2, \dots, \mathbf{n}_P].\end{aligned}\tag{4.3}$$

In array signal processing, the column space of the matrix \mathbf{E} in (4.2) is called the signal subspace [69]. In this dissertation, the signal subspaces are called the lesion and normal tissue subspaces which are denoted as $\langle \mathbf{H} \rangle$ and $\langle \mathbf{S} \rangle$, respectively, where $\langle \mathbf{H} \rangle$ is the subspace spanned by the columns of the $N \times p$ matrix \mathbf{H} , $\langle \mathbf{S} \rangle$ is the subspace spanned by the columns of the $N \times t$ matrix \mathbf{S} , and $p + t < N$. Based on the compartmental model analysis, the subspaces $\langle \mathbf{H} \rangle$ and $\langle \mathbf{S} \rangle$ have the input plasma subspace in common, otherwise, they are linearly independent in which case the columns of the concatenated matrix $[\mathbf{HS}]$ span the $(p + t)$ -dimensional subspace $\langle \mathbf{HS} \rangle$.

4.3 Subspace Identification from Known Tissue Type

Two categories of subspace identification methods are used in this dissertation, namely, *non-parametric* and *parametric* methods, for solving the signal-subspace-fitting problem. The non-parametric techniques used here simply decompose the observed data to extract the subspaces using a singular value decomposition method. The parametric method is used to estimate the parameters of interest in spectrum-like functions, e.g., least squares estimation for the exponential parameters in Eq. (3.7).

4.3.1 Non-Parametric: Singular Value Decomposition

The non-parametric methods find a multidimensional signal subspace by a simple eigen-decomposition of the autocorrelation matrix or a singular value decomposition of the data matrix. The SVD method is used in this dissertation to estimate the physiological factors defined in Eq. (3.17). Given that the coefficient matrix \mathbf{A} in Eq. (4.2) is uncorrelated with the noise \mathbf{N} which is assumed to be white, the autocorrelation matrix of the data \mathbf{Y} can be decomposed as follows:

$$\begin{aligned}
 \mathbf{R}_Y &= \mathbf{Y}\mathbf{Y}^T \\
 &= \mathbf{H}\mathbf{A}\mathbf{A}^T\mathbf{H} + \sigma_n^2\mathbf{I} \\
 &= \Phi[\Lambda + \sigma_n^2\mathbf{I}]\Phi^T \\
 &= \Phi_s\Lambda_s\Phi_s^T + \Phi_n\Lambda_n\Phi_n^T
 \end{aligned} \tag{4.4}$$

where we assume that $\mathbf{A}\mathbf{A}^T$, is a full rank matrix, and therefore $\mathbf{H}\mathbf{A}\mathbf{A}^T\mathbf{H}^T$ can be eigendecomposed as $\Phi_s\Lambda_s\Phi_s^T$ such that $\langle\mathbf{H}\rangle=\langle\Phi_s\rangle$. The r eigenvalues of the decomposition combine with the noise covariance to form the $r \times r$ diagonal matrix $\Lambda_s = \Lambda + \sigma_n^2\mathbf{I}$, with the eigenvalues in Λ_s arranged in decreasing order. The $(N - r) \times (N - r)$ diagonal matrix Λ_n contains the $N - r$ repeated eigenvalues σ_n^2 . Thus

the eigen-decomposition of the data autocorrelation matrix in Eq. (4.4) results in a signal subspace Φ_s and a noise-only subspace Φ_n .

4.3.2 Parametric: Least Squares Estimation

Finding the subspace using the parametric algorithm is equivalent to the estimation of the exponential basis in Eq. (3.7), which is similar to the well-known problem of finding the direction of arrival (DOA) in signal subspace processing [69]. In this dissertation, the least squares (LS) method is applied for the parametric method and the best fit of parameters to the observed data are chosen to constitute the subspaces. Subspace fitting using the LS method is defined as [69]:

$$\hat{\mathbf{H}}, \hat{\mathbf{A}} = \arg \min_{\mathbf{H}, \mathbf{A}} \|\mathbf{Y} - \mathbf{H}\mathbf{A}\|_F^2 \quad (4.5)$$

where $\|\cdot\|_F$ denotes the Frobenius norm. Because the subspace fitting problem is separable in \mathbf{H} and \mathbf{A} [69], by substituting the pseudoinverse solution, $\hat{\mathbf{A}} = (\mathbf{H}^T \mathbf{H})^{-1} \mathbf{H}^T \mathbf{Y}$, back into Eq. (4.5), the following equivalent problem is derived:

$$\begin{aligned} \hat{\mathbf{H}} &= \arg \min_{\mathbf{H}} \|\mathbf{Y} - \mathbf{H}(\mathbf{H}^T \mathbf{H})^{-1} \mathbf{H}^T \mathbf{Y}\|_F^2 \\ &= \arg \min_{\mathbf{H}} \|\mathbf{P}_H^\perp \mathbf{Y}\|_F^2 \\ &= \arg \max_{\mathbf{H}} \|\mathbf{P}_H \mathbf{Y}\|_F^2 \end{aligned}$$

$$= \arg \max_{\mathbf{H}} \text{tr}\{\mathbf{P}_H \mathbf{Y} \mathbf{Y}^T\} \quad (4.6)$$

where $\mathbf{P}_H = \mathbf{H}(\mathbf{H}^T \mathbf{H})^{-1} \mathbf{H}^T$ is the orthogonal projection matrix that projects onto the column space of \mathbf{H} and “tr” means the trace operator. In feature identification using parametric algorithm for a FDG-PET dynamic study, the only unknowns are the exponential parameters, the LS method becomes to search the parameters over a reasonable range for the tracer kinetic parameters.

4.3.3 Subspace Refining: A Subspace Distance Measure

The lesion and normal tissue subspaces estimated *individually* by the parametric or non-parametric methods from the known types of tissue data generally capture the characteristics of lesion and normal tissues, respectively. But from the physiological compartmental model analysis, the resulting two subspaces, containing the common input plasma subspace, may be so close to each other that they can hardly be separated. Hence, to improve the lesion detection performance (see Chapter 5), a subspace correlation method is used to refine the identified subspaces.

The subspace refining procedure selects two subsets of basis vectors (column vectors) from the identified subspaces $\langle \mathbf{H} \rangle$ and $\langle \mathbf{S} \rangle$ based on subspace distance maximization between the two candidate subsets, subject to the condition that the LSE

are less than given values. By the process of refining, the common input plasma function will be excluded from both lesion and normal tissue subspaces.

By a subspace distance measure, the subspace refining can be described as: given the identified subspaces $\langle \mathbf{H} \rangle$ and $\langle \mathbf{S} \rangle$,

$$\begin{aligned} \mathbf{H}', \mathbf{S}' = \arg \max_{\mathbf{H}, \mathbf{S}} distance \{ \mathbf{H}, \mathbf{S} \} \\ \text{subject to } \begin{cases} ||\mathbf{Y} - \mathbf{P}_{H'} \mathbf{Y}||_F < \epsilon_1 \\ ||\mathbf{Y} - \mathbf{P}_{S'} \mathbf{Y}||_F < \epsilon_2 \end{cases} \end{aligned} \quad (4.7)$$

where $distance \{ \mathbf{H}, \mathbf{S} \} \triangleq \sqrt{1 - r_1^2}$ is the subspace distance, where r_1 is the largest principal correlation coefficient between \mathbf{H} and \mathbf{S} [21], and ϵ_1 and ϵ_2 are the thresholds set for achieving the fidelity criterion.

Chapter 5

Matched Subspace Detector

5.1 Overview

After identifying the lesion and normal tissue subspaces using the methods described in Chapter 4, how to incorporate the identified subspaces into statistical decision criteria becomes critical and will be addressed in this Chapter. The generalized likelihood ratio test (GLRT) is a standard procedure for solving the detection problem [55, 75, 76, 77, 78]. The GLRT is used to derive the matched subspace detector which is the general building block of multi-rank matched filter in signal processing. In sonar signal processing, the matched subspace detector is also called a matched field detector [54]. Generally, the matched subspace detectors turn out to be a ratio of generalized energy detectors.

In this Chapter, three types of GLRTs will be derived under different assumption of voxel spatial correlation. The first GLRT directly applies the algorithm developed in [55] by assuming that pixels are spatially uncorrelated. Both additive and replacement noise models are used to characterize the observations of large lesions and small lesions in this approach. Considering that image pixel values are not statistically uncorrelated because each count contributes to all pixel values [7], the second GLRT adds a pre-whitening procedure to the first. The spatial covariance matrix required for the pre-whitening process is to be computed using the methods described in Appendix B [7, 30, 31]. Finally, the third detector extends the GLRT criterion to a multi-pixel detection. In this approach, it is assumed that the spatial inter-pixel correlation in each frame has the same structure but different energy level.

5.2 Hypothesized Data Model

In this dissertation, depending on the size of lesions, two data models are applied for the detection hypothesis, namely, the replacement model and the superimposed model.

5.2.1 Replacement Model

Based on a replacement model, which is used to model a large lesion in FDG-PET images, *two* possible hypotheses regarding how the PET data was generated are needed. The null hypothesis H_0 says that the data consists of a sum of normal tissue signal \mathbf{x}_0 and noise \mathbf{n}_0 . The alternate hypothesis H_1 says that the data consist of a sum of lesion signal \mathbf{x}_1 and noise \mathbf{n}_1 . That is

$$\begin{cases} H_0 : \mathbf{y} = \mathbf{x}_0 + \mathbf{n}_0 \\ H_1 : \mathbf{y} = \mathbf{x}_1 + \mathbf{n}_1 \end{cases} \quad (5.1)$$

where the signal \mathbf{x}_i is assumed to obey the linear subspace model

$$\begin{aligned} \mathbf{x}_0 &= \mathbf{S}\phi, \quad \mathbf{S} \in \mathcal{R}^{N \times t}, \quad \phi \in \mathcal{R}^t, \\ \mathbf{x}_1 &= \mathbf{H}\theta, \quad \mathbf{H} \in \mathcal{R}^{N \times p}, \quad \theta \in \mathcal{R}^p, \quad t < N - p. \end{aligned} \quad (5.2)$$

5.2.2 Superimposed Model

For the small lesion case, partial volume effects will cause the lesion signal to be mixed with the background normal tissue signal, hence, it is best represented by a

superimposed model. To model the small lesion case, the superimposed model is used for the hypothesis H_i which are given by

$$\begin{cases} H_0 : \mathbf{y} = \mathbf{x}_{00} + \mathbf{n}_0 \\ H_1 : \mathbf{y} = \mathbf{x}_1 + \mathbf{x}_{01} + \mathbf{n}_1 \end{cases} \quad (5.3)$$

where the linear model for the \mathbf{x}_1 (lesion signal) and \mathbf{n}_i are the same as those defined in the replacement model and

$$\begin{aligned} \mathbf{x}_{00} &= \mathbf{S}\phi_0, \phi_0 \in \mathcal{R}^t, \text{ under hypothesis } H_0 \\ \mathbf{x}_{01} &= \mathbf{S}\phi_1, \phi_1 \in \mathcal{R}^t, \text{ under hypothesis } H_1. \end{aligned} \quad (5.4)$$

5.3 GLRT: Spatially Uncorrelated Assumption

5.3.1 Replacement Model

Based on the spatially uncorrelated assumption, the noise \mathbf{n}_i can be modeled as normal with zero mean and covariance matrix $\sigma_i^2 \mathbf{I}$. Then, the detection problem for the replacement model becomes a test of the distributions:

$$\begin{cases} H_0 : \mathbf{y} = \mathbf{x}_0 + \mathbf{n}_0 : N[\mathbf{S}\phi, \sigma_0^2 \mathbf{I}] \\ H_1 : \mathbf{y} = \mathbf{x}_1 + \mathbf{n}_1 : N[\mathbf{H}\theta, \sigma_1^2 \mathbf{I}]. \end{cases} \quad (5.5)$$

The likelihood ratio test can be written as

$$l(\mathbf{y}) = \frac{l(\theta, \sigma_1^2; \mathbf{y})}{l(\phi, \sigma_0^2; \mathbf{y})}$$

$$= \left(\frac{\sigma_1^2}{\sigma_0^2} \right)^{-N/2} \exp \left\{ -\frac{1}{2\sigma_1^2} \|\mathbf{n}_1\|_2^2 + \frac{1}{2\sigma_0^2} \|\mathbf{n}_0\|_2^2 \right\}. \quad (5.6)$$

Hence, the *generalized likelihood ratio test* (GLRT) can be derived by substituting the maximum likelihood estimate (MLE) of \mathbf{n}_i , $\boldsymbol{\theta}$ and $\boldsymbol{\phi}$:

$$\begin{aligned} \hat{l}(\mathbf{y}) &= \frac{l(\hat{\boldsymbol{\theta}}, \hat{\sigma}_1^2; \mathbf{y})}{l(\hat{\boldsymbol{\phi}}, \hat{\sigma}_0^2; \mathbf{y})} \\ &= \left(\frac{\hat{\sigma}_1^2}{\hat{\sigma}_0^2} \right)^{-N/2} \exp \left\{ -\frac{1}{2\hat{\sigma}_1^2} \|\hat{\mathbf{n}}_1\|_2^2 + \frac{1}{2\hat{\sigma}_0^2} \|\hat{\mathbf{n}}_0\|_2^2 \right\}. \end{aligned} \quad (5.7)$$

The MLE, $\hat{\mathbf{n}}_i$, $\hat{\boldsymbol{\theta}}$, and $\hat{\boldsymbol{\phi}}$, can be written as

$$\begin{aligned} \hat{\boldsymbol{\phi}} &= (\mathbf{S}^T \mathbf{S})^{-1} \mathbf{S}^T \mathbf{y} \\ \hat{\boldsymbol{\theta}} &= (\mathbf{H}^T \mathbf{H})^{-1} \mathbf{H}^T \mathbf{y} \\ \hat{\mathbf{n}}_0 &= \mathbf{y} - \mathbf{S} \hat{\boldsymbol{\phi}} = \mathbf{y} - \mathbf{S} (\mathbf{S}^T \mathbf{S})^{-1} \mathbf{S}^T \mathbf{y} = \mathbf{P}_S^\perp \mathbf{y} \\ \hat{\mathbf{n}}_1 &= \mathbf{y} - \mathbf{H} \hat{\boldsymbol{\theta}} = \mathbf{y} - \mathbf{H} (\mathbf{H}^T \mathbf{H})^{-1} \mathbf{H}^T \mathbf{y} = \mathbf{P}_H^\perp \mathbf{y} \end{aligned} \quad (5.8)$$

where \mathbf{P}_H^\perp is the orthogonal projection onto the complement subspace of $\langle \mathbf{H} \rangle$. Because σ_i^2 is unknown and the MLE of σ_i^2 is $\hat{\sigma}_i^2 = \frac{1}{N} \|\hat{\mathbf{n}}_i\|_2^2$, it is more convenient to replace the GLRT by the $(N/2)$ -root GLRT. Hence, the GLRT for the replacement hypothesis model becomes

$$L_r(\mathbf{y}) = [\hat{l}(\mathbf{y})]^{2/N} = \frac{\|\hat{\mathbf{n}}_0\|_2^2}{\|\hat{\mathbf{n}}_1\|_2^2}$$

$$= \frac{\mathbf{y}^T \mathbf{P}_S^\perp \mathbf{y}}{\mathbf{y}^T \mathbf{P}_H^\perp \mathbf{y}}. \quad (5.9)$$

5.3.2 Superimposed Model

Under the spatially uncorrelated assumption, the detection problem for superimposed model is a test of the distributions:

$$\begin{cases} H_0 & : \mathbf{y} = \mathbf{x}_{00} + \mathbf{n}_0 & : N[\mathbf{S}\phi_0, \sigma_0^2 \mathbf{I}] \\ H_1 & : \mathbf{y} = \mathbf{x}_1 + \mathbf{x}_{01} + \mathbf{n}_1 & : N[\mathbf{H}\boldsymbol{\theta} + \mathbf{S}\phi_1, \sigma_1^2 \mathbf{I}]. \end{cases} \quad (5.10)$$

Hence, the GLRT can be expressed as

$$\begin{aligned} \hat{l}(\mathbf{y}) &= \frac{l(\hat{\boldsymbol{\theta}}, \hat{\phi}_1, \hat{\sigma}_1^2; \mathbf{y})}{l(\hat{\phi}_0, \hat{\sigma}_0^2; \mathbf{y})} \\ &= \left(\frac{\hat{\sigma}_1^2}{\hat{\sigma}_0^2} \right)^{-N/2} \exp \left\{ -\frac{1}{2\hat{\sigma}_1^2} \|\hat{\mathbf{n}}_1\|_2^2 + \frac{1}{2\hat{\sigma}_0^2} \|\hat{\mathbf{n}}_0\|_2^2 \right\}. \end{aligned} \quad (5.11)$$

The MLE $\hat{\mathbf{n}}_0$ is the same as that derived in the replacement model, i.e.,

$$\hat{\mathbf{n}}_0 = \mathbf{P}_S^\perp \mathbf{y}. \quad (5.12)$$

For the $\hat{\mathbf{n}}_1$, because the MLE of $\boldsymbol{\theta}$ and ϕ_1 are given by

$$\begin{aligned} \begin{bmatrix} \hat{\boldsymbol{\theta}} \\ \hat{\phi}_1 \end{bmatrix} &= [\mathbf{H} \ \mathbf{S}]^\# \mathbf{y} = ([\mathbf{H} \ \mathbf{S}]^T [\mathbf{H} \ \mathbf{S}])^{-1} [\mathbf{H} \ \mathbf{S}]^T \mathbf{y} \\ &= \begin{bmatrix} \mathbf{H}^T \mathbf{H} & \mathbf{H}^T \mathbf{S} \\ \mathbf{S}^T \mathbf{H} & \mathbf{S}^T \mathbf{S} \end{bmatrix}^{-1} \begin{bmatrix} \mathbf{H}^T \\ \mathbf{S}^T \end{bmatrix} \mathbf{y} \end{aligned}$$

$$= \begin{bmatrix} (\mathbf{H}^T \mathbf{P}_S^\perp \mathbf{H})^{-1} \mathbf{H}^T \mathbf{P}_S^\perp \\ (\mathbf{S}^T \mathbf{P}_H^\perp \mathbf{S})^{-1} \mathbf{S}^T \mathbf{P}_H^\perp \end{bmatrix} \mathbf{y} \quad (5.13)$$

and from Eq. (A.5) in Appendix A, then

$$\begin{aligned} \hat{\mathbf{n}}_1 &= \mathbf{y} - \mathbf{H}\hat{\boldsymbol{\theta}} - \mathbf{S}\hat{\boldsymbol{\phi}}_1 \\ &= \mathbf{y} - \mathbf{H}(\mathbf{H}^T \mathbf{P}_S^\perp \mathbf{H})^{-1} \mathbf{H}^T \mathbf{P}_S^\perp \mathbf{y} - \mathbf{S}(\mathbf{S}^T \mathbf{P}_H^\perp \mathbf{S})^{-1} \mathbf{S}^T \mathbf{P}_H^\perp \mathbf{y} \\ &= \mathbf{y} - \mathbf{E}_{HS} \mathbf{y} - \mathbf{E}_{SH} \mathbf{y} \\ &= \mathbf{P}_{HS}^\perp \mathbf{y} \end{aligned} \quad (5.14)$$

where \mathbf{E}_{HS} and \mathbf{E}_{SH} are called the oblique projections defined in Appendix A. Therefore, the $(N/2)$ -root GLRT for the superimposed model becomes

$$\begin{aligned} L_s(\mathbf{y}) &= [\hat{l}(\mathbf{y})]^{2/N} = \frac{\|\hat{\mathbf{n}}_0\|_2^2}{\|\hat{\mathbf{n}}_1\|_2^2} \\ &= \frac{\mathbf{y}^T \mathbf{P}_S^\perp \mathbf{y}}{\mathbf{y}^T \mathbf{P}_{HS}^\perp \mathbf{y}}. \end{aligned} \quad (5.15)$$

Note that the matrices \mathbf{H} and \mathbf{S} used to derived the above GLRTs for both replacement and superimposed models are assumed independent (after subspace angle refining). In Appendix C, we showed that the GLRTs can not be improved by further projecting the lesion subspace $\langle \mathbf{H} \rangle$ onto the orthogonal complement subspace of the normal tissue subspace $\langle \mathbf{S} \rangle$. The GLRTs for the superimposed model are exactly

the same before and after using the orthogonal refined subspaces. For the replacement model, The GLRT is degraded after using the refined orthogonal subspaces. In summary, the GLRT can not be improved if two orthogonal subspaces are defined.

5.4 Spatially Correlated Assumption

5.4.1 Local Statistics Computation

It is known that image pixel values are not statistically uncorrelated because each count contributes to all pixel values [7]. Hence, a decorrelation for the pre-whitening process is important before applying the GLRT. The decorrelation procedure requires the computation of a covariance matrix in the ROI. The covariance matrix can be estimated by simply averaging the samples around the ROI. However, this sample-averaging method to compute the local statistics can be poor since the local statistics assumption required may be invalid [27, 79]. Calculation accuracy can be guaranteed by using the formulas developed in [7, 19, 30, 31] which exploit the Poisson data model for a PET system. The linear and non-linear covariance computation methods for the FBP and MAP reconstructed images, respectively, are described in Appendix B, and are used here to estimate the inter-pixel covariance, frame by frame.

5.4.2 GLRT

Because of the spatially correlated assumption, the average of TACs over an ROI may enhance rather than suppress the observation noise. Thus, to mitigate this, the TAC-averaging is preceded by a spatial decorrelation operation before applying the GLRT. This spatial decorrelation is usually called a pre-whitening procedure.

5.4.3 Multi-Pixel GLRT

In this subsection, the GLRT criterion is extended to multi-pixel GLRT detection. In this approach, it is assumed that the spatial inter-pixel correlation in each frame has the same structure but different energy level. Let the P -dimensional vector $\mathbf{f}_i = [f_i(1), f_i(2), \dots, f_i(P)]^\top$ denote the spatial pixel data for the i -th frame and denote $\mathbf{F} = [\mathbf{f}_1, \mathbf{f}_2, \dots, \mathbf{f}_N]$. We assume that all the columns of the matrix \mathbf{F} are independent. Hence $\mathbf{Y} \triangleq [\mathbf{y}_1, \mathbf{y}_2, \dots, \mathbf{y}_P] = \mathbf{F}^\top$. The derivation of the multi-pixel GLRT for the constrained correlation structure is based on a replacement model, i.e.,

$$\begin{cases} H_0 : \mathbf{Y} = \mathbf{X}_0 + \mathbf{N}_0 \\ H_1 : \mathbf{Y} = \mathbf{X}_1 + \mathbf{N}_1. \end{cases} \quad (5.16)$$

The GLRT can be derived as (see Appendix B):

$$l_3(\mathbf{Y}) = \frac{1 + (\mathbf{G}^{-1/2} \mathbf{R} \tilde{\mathbf{s}})^\top \mathbf{P}_{\tilde{\mathbf{S}}}^\perp (\mathbf{G}^{-1/2} \mathbf{R} \tilde{\mathbf{s}})}{1 + (\mathbf{G}^{-1/2} \mathbf{R} \tilde{\mathbf{s}})^\top \mathbf{P}_{\tilde{\mathbf{H}}}^\perp (\mathbf{G}^{-1/2} \mathbf{R} \tilde{\mathbf{s}})} \quad (5.17)$$

where $\mathbf{G} \triangleq \mathbf{R}\mathbf{R}^\top - (\mathbf{R}\tilde{\mathbf{s}})(\mathbf{R}\tilde{\mathbf{s}})^\top$, \mathbf{R} is the covariance matrix, and $\tilde{\mathbf{s}} \triangleq (\mathbf{s}^\top \mathbf{s})^{1/2} \mathbf{s}$,
 $\mathbf{s}^\top \triangleq \mathbf{1}^\top \mathbf{M}^{-1/2}$. The matrix \mathbf{M} is the correlation structure for each frame.

Chapter 6

Experiment and Result

In this Chapter, experiments and results for dynamic feature identification and lesion detection in FDG-PET dynamic study are presented. Both clinical and phantom dynamic data will be used in this dissertation. For the clinical dynamic data, two cases will be demonstrated, including one lung cancer dynamic study and one breast cancer dynamic study. Each study contains one confirmed primary lesion which will be used for lesion subspace estimation, and one small lesion which will be used for the subspace fidelity and GLRT demonstration. For the breast cancer dynamic study, there is one “unknown” small lesion which can not be confirmed by eye, but is successfully enhanced after applying the GLRT. For the phantom data, two phantoms, one with five artificial lesions inserted and the other with only pure normal tissue background (no lesion), are generated. The time activity curves (TAC) of a lesion and normal tissues observed from the clinical lung cancer dynamic data are

used to simulate the dynamics for the phantom. To calculate the local statistics for the pre-whitening purpose, the methods [7, 19, 30, 31] described in Appendix B will be applied for covariance computation. A receiver operating characteristic (ROC) study for the GLRT performance will be presented based on the dynamic phantom study.

6.1 Protocol of FDG-PET Dynamic Study

The clinical FDG-PET dynamic data was acquired with a Siemens/CTI ECAT Model 953A whole-body PET scanner. This device provides 31 contiguous transaxial image planes with an axial field of view of 10.8 cm. The nominal intrinsic resolution of the system is 4 mm in all 3 dimensions. Consecutive detector rings are separated by tungsten septa in order to reduce scatter noise. Dynamic data was acquired from 0 to 55 minute post injection. The final 10 minute frame can be used in place of the routine static study used in purely clinical examinations. The dynamic structure protocol for the clinical data acquisition is listed in Table 6.1. Based on this protocol, an FDG-PET dynamic study contains 36 frames for a fixed plane position.

Scan Type	Scan Times	Frame Duration
Dynamic scan	0 - 2 min	15 sec/frame
Dynamic scan	3 - 5 min	30 sec/frame
Dynamic scan	6 - 25 min	1 min/frame
Dynamic scan	26 - 45 min	5 min/frame
Static scan	45 - 55 min	10 min

Table 6.1: Dynamic data acquisition protocol

6.2 Clinical Study

Two clinical FDG-PET dynamic studies, one lung cancer study and one breast cancer study, will be used in this dissertation. Each study contains one confirmed primary lesion which will be applied for lesion subspace estimation and one small lesion which will be used for the subspace fidelity and GLRT demonstration. The last frame image reconstructed from the FBP method is shown in Figure 6.1: (a) and (b) for the lung cancer study and the breast cancer image, respectively.

An ROI, indicated by a rectangle, can be drawn over a segment of the tissue on the dynamic FDG-PET images and then duplicated to all frames, so that the activity in that tissue can be tracked over time. The advantage of the ROI method over a single pixel is that it is less sensitive to noise and typically results in a smaller error in the parameter estimates. Data obtained through ROI analysis of dynamic images produces a tissue time activity curve (TAC). This curve represents

the counts/second/pixel (or counts/second/ml, if calibration data is available) in a given region as a function of time. Figure 6.1: (c) and (d) shows examples of TAC for the two clinical dynamic studies.

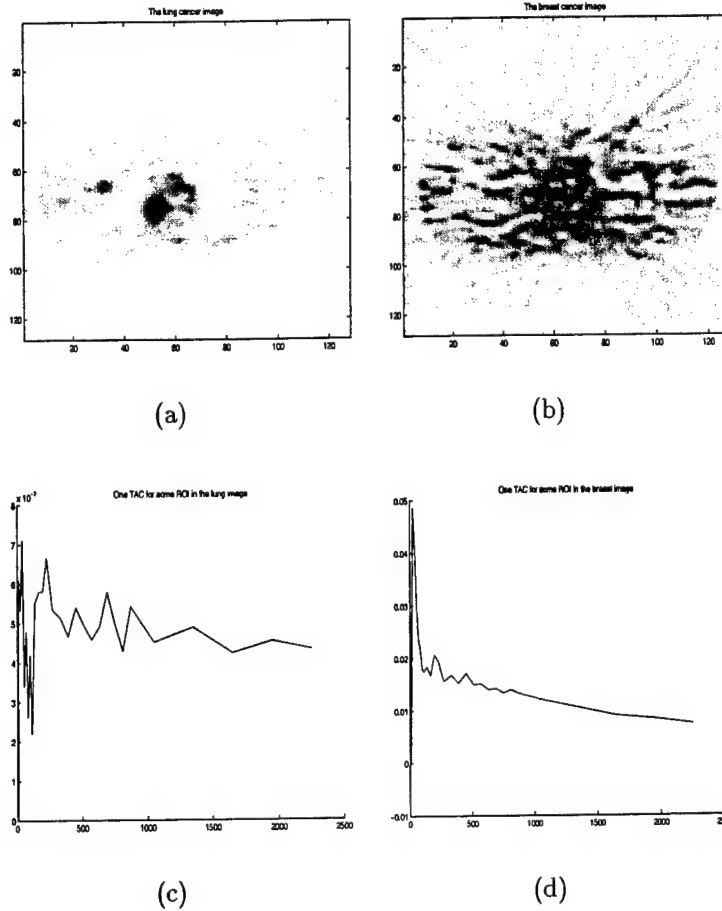


Figure 6.1: Clinical dynamic studies used in this dissertation: (a) the lung cancer image (FBP), (b) the breast cancer image (FBP), (c) one TAC example from the lung cancer dynamic study, (d) one TAC example from the breast cancer dynamic study.

6.2.1 Lung Cancer FDG-PET Dynamic Study

In the lung cancer FDG-PET dynamic study, two lesions, one primary (large and clearly visualized) and the other a metastasis (smaller and barely seen), in a lung cancer patient with multiple metastases, are indicated in Figure 6.2 (a). Three 5×5 pixel ROIs, L1, L2, and BG, indicated in Figure 6.2 (a), were selected from the primary lesion, the metastasis lesion, and the normal lung tissue, respectively. Their corresponding TACs are plotted in Figure 6.2 (b) where the TACs from the L1 and L2 both have the trend to increase with time while the BG TAC does not. This demonstrates the property of FDG kinetics to show differential uptake in lesions and normal tissue.

6.2.1.1 Subspace Estimation

The TACs observed from the L1 and BG ROIs in Figure 6.2 (b) were used to form the temporal-spatial data matrices for identifying the lesion and normal tissue subspaces, $\langle \mathbf{H} \rangle$ and $\langle \mathbf{S} \rangle$, respectively.

For the parametric method, the LS search algorithm was used. For this lung cancer study, the TAC subspaces of normal lung tissue and lung cancer estimated by the LS method were found to be spanned by the exponential basis $\{e^{-\theta_1 t}, e^{-\theta_2 t}, e^{-\theta_3 t}\}$ and $\{1 - e^{-\beta_1 t}, e^{-\beta_2 t}, te^{-\beta_3 t}\}$, respectively, and the parameter sets were $\{\theta_1 = 0.00025,$

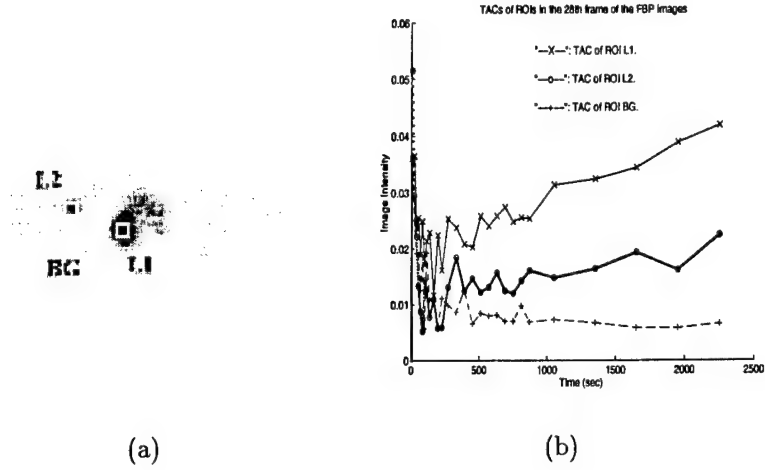


Figure 6.2: Test image reconstructed from FBP: (a) the last frame of the dynamic FDG-PET FBP reconstructed images, where three ROIs were chosen: L1 in the big lesion, L2 in the small lesion, and BG in the background, (b) the corresponding TACs for L1, L2, and BG, respectively.

$\theta_2 = 0.005, \theta_3 = 0.05\}$ and $\{\beta_1 = 0.005, \beta_2 = 0.0223, \beta_3 = 0.00125\}$ for BG and L1, respectively. For the non-parametric method, we applied the SVD method, where the data correlation matrix was estimated using the temporal-spatial data matrix formed from L1 and BG ROIs. The eigenvectors corresponding to the first $d1$ and $d2$ significant eigenvalues of the two estimated correlation matrices were chosen to span the TAC subspaces of the lung cancer and normal lung tissues, respectively. In our study, $d1 = d2 = 2$.

The accuracy (fidelity) of the lesion subspace estimated using the primary lung tumor was examined by projecting the observed L1 and L2 TACs onto the estimated

lesion subspace. Also, the accuracy of the normal tissue subspace estimated using the BG ROI was examined by projecting the observed BG TAC onto the estimated normal tissue subspace. On the other hand, the separability of the subspace was examined by projecting the L1 and L2 TACs onto the normal tissue subspace, and by projecting the BG TAC onto the L1 subspace. The results from the LS method and the SVD method are shown in Figure 6.3. It was demonstrated that the TAC of the metastatic lesion can be represented by the subspace features extracted from the big lesion with a high accuracy in both methods, and that a large separability exists between the lesion subspace and the normal lung tissue subspace.

6.2.1.2 GLRT

A test region which includes the small lesion and some part of the primary lesion was selected as indicated by a rectangle in Figure 6.4 (a). The GLRT (white noise assumption) with either a superimposed or a replacement data hypothesis model in Eqs. (5.9) and (5.15) was used to perform a multiple pixel test for each 5×5 pixel ROI contained in the test region. The corresponding GLRT result is shown in Figure 6.4 (c)-(e) which indicates that the matched subspace detection incorporated with the lesion and normal tissue subspaces extracted by the SVD method and the

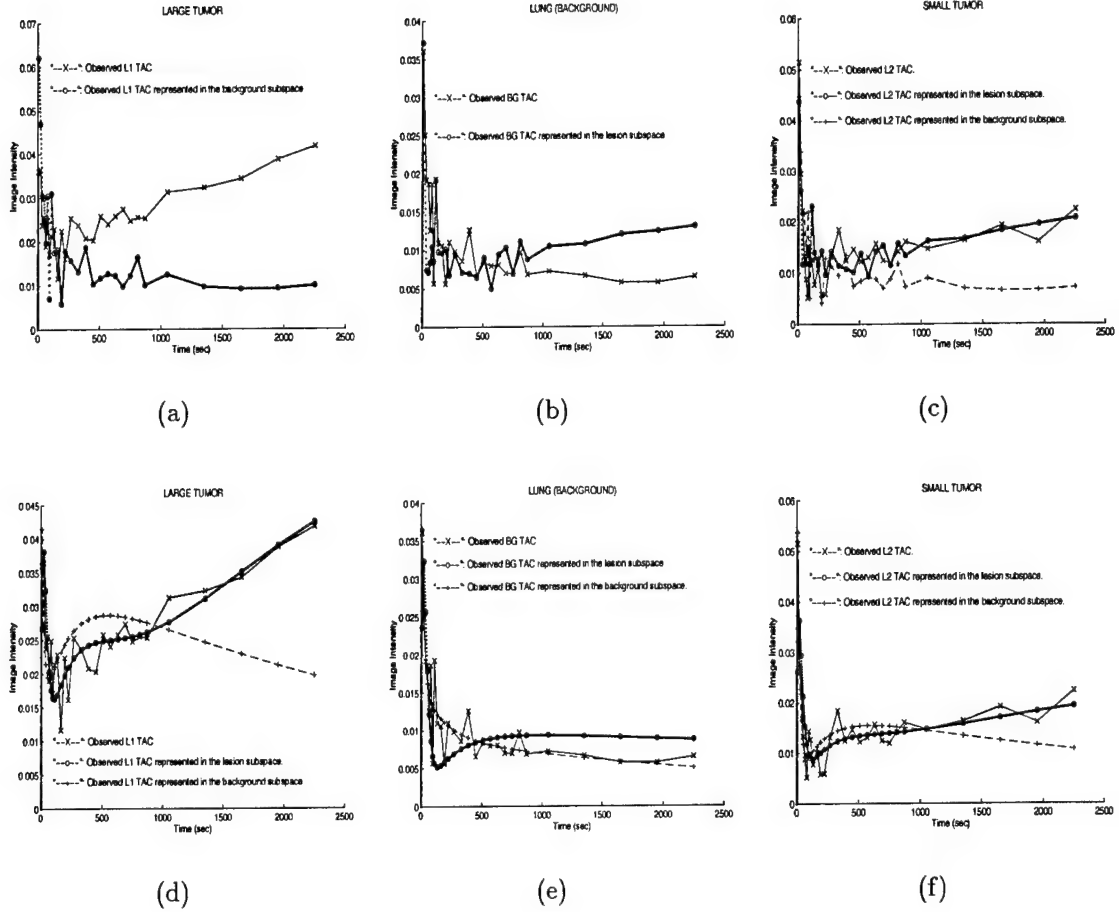


Figure 6.3: Comparison of accuracy and separability of extracted subspaces of TACs in lesions and normal tissue by the SVD method: (a) TAC in L1 represented by the normal tissue subspace, (b) TAC in BG represented by the lesion subspace, (c) TAC in L2 represented by the lesion and normal tissue subspaces, respectively. Comparison of accuracy and separability of extracted subspaces of TACs in lesions and normal tissue by the LS method: (d) TAC in L1 represented by the normal tissue subspace, (e) TAC in BG represented by the lesion subspace, (f) TAC in L2 represented by the lesion and background subspaces, respectively.

LS method significantly increases the lesion-to-normal tissue contrast for the small lesion relative to the original FBP image in Figure 6.4 (b).

Another test region was selected to include the heart area in order to demonstrate suppression of activity in the heart by the GLRT. Figure 6.5 (a) shows the selected test region in the lung cancer dynamic study, where the primary lesion, the small lesion, and the heart area were all included. Figure 6.5 (b) shows the original 3-D mesh of the test region. The GLRT of the test region is shown in Figure 6.5 (c), where the heart activity is suppressed significantly after applying the GLRT.

In order to apply the whitening process for the spatially uncorrelated FBP data, we used the method proposed by Carson [7] to calculate the spatial covariance matrix. Carson's approximation formula assumes that the ROI is smooth and the pixel variances inside the ROI are similar. Therefore, the covariance matrix is just a function of the filter and the location of the pixels. The advantage of Carson's formula is that it does not need access to the original projection data and is convenient for routine use. See Appendix B for more details. Figure 6.6 shows the results of the GLRT for the FBP image after applying the estimated covariance matrix.

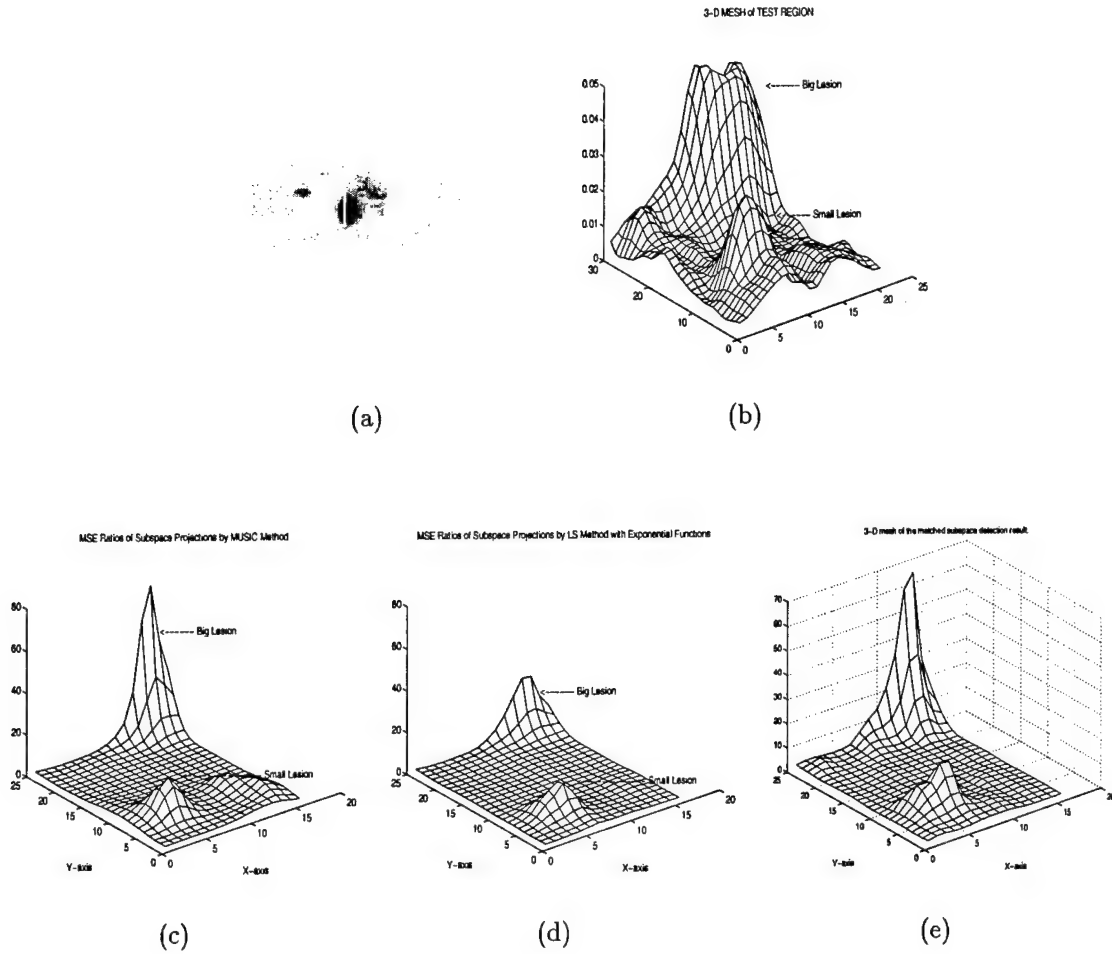
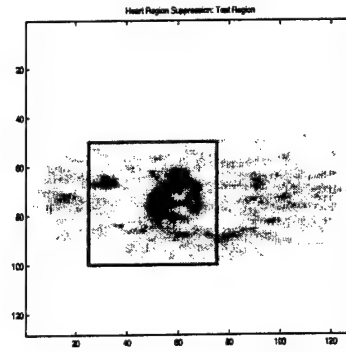
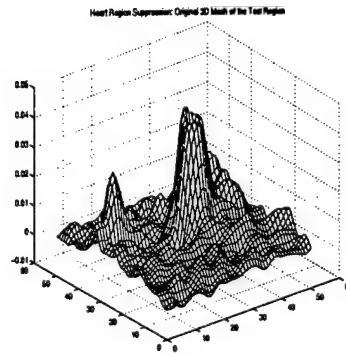


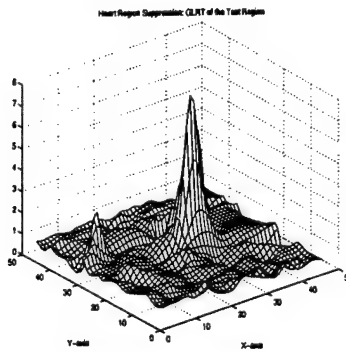
Figure 6.4: (a) The last frame of the dynamic FDG-PET FBP reconstructed images, where a rectangle indicates a test region containing a part of the big lesion and the whole small lesion, (b) 3-D mesh of the test region indicated in (a), (c) GLRT with replacement model for TAC subspaces obtained by the SVD method, (d) GLRT with replacement model for TAC subspaces obtained by the LS method, (e) GLRT with superimposed model for TAC subspaces obtained by the LS method.



(a)



(b)



(c)

Figure 6.5: (a) The test region indicated by a rectangle in the lung cancer study, where the primary lesion, the small lesion, and the heart area were all included. (b) 3-D mesh of the original test region. (c) The result of the GLRT.

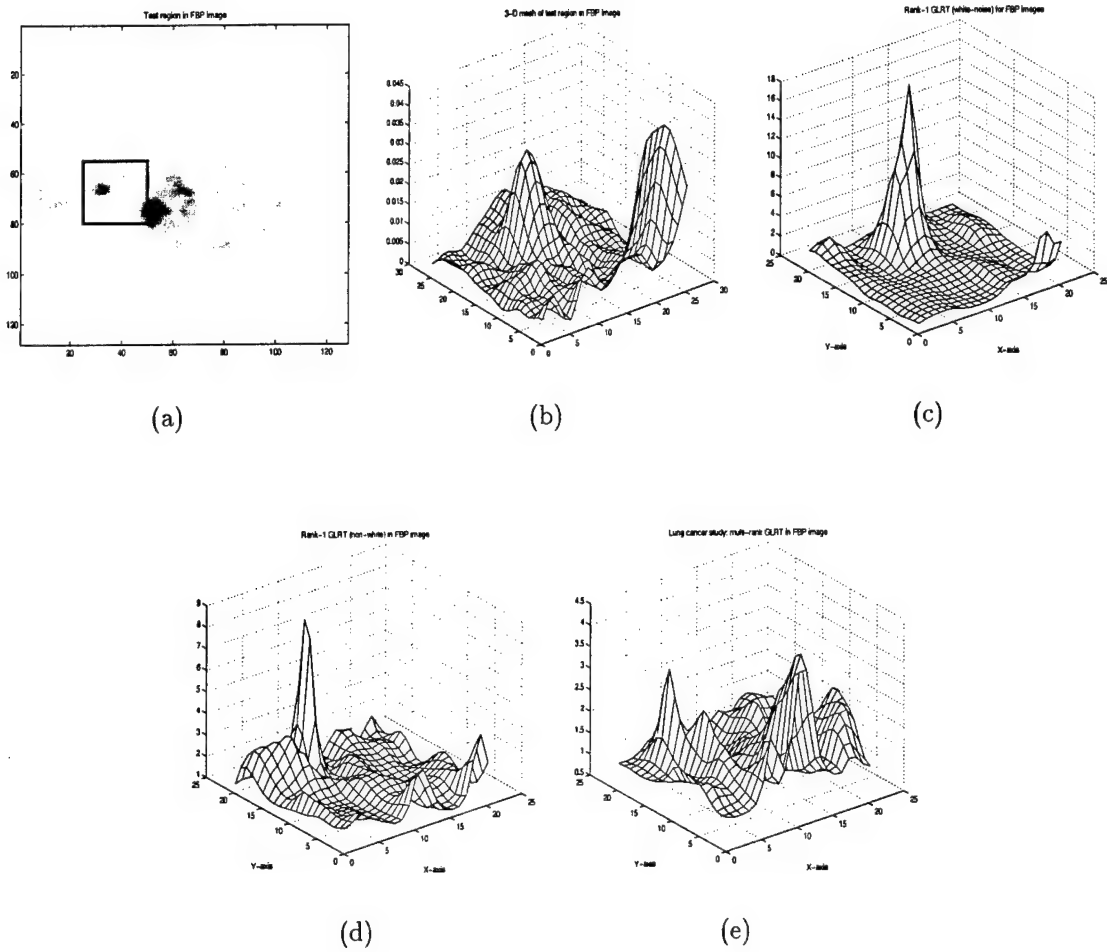


Figure 6.6: (a) The test region indicated by a rectangle in the lung cancer study. (b) 3-D mesh of the original test region. (c) GLRT (white noise). (d) GLRT (non-white). (e) Multi-pixel GLRT.

6.2.1.3 Subspace Refining Method

For the proposed subspace refining algorithm described by Eq. (4.7), we estimated four LS TAC bases for both lesion and normal tissue subspaces, and used the subspace refining algorithm to retain only three bases for both subspaces. Figure 6.7 (a) and (b) shows the fidelity between the estimated TAC by the identified subspaces and the observed TAC without subspace refining (four bases) and Figure 6.7 (c) shows the GLRT. The corresponding results after subspace refining (three bases retained) are shown in Figure 6.7 (d), (e), and (f), respectively, where not only the fidelity was preserved, but also the GLRT performance is significantly improved.

For the orthogonal projection, we already showed, see Appendix C, that the refined subspaces by the orthogonal projection can not improve the GLRT with the original estimated subspaces. The experimental results are as follows. Figure 6.8 (a) and (b) show the test region chosen and its corresponding 3-D mesh. Figure 6.8 (c) and (d) show the GLRTs for the superimposed model before and after using the orthogonal refined subspaces, where the two GLRTs were exactly the same. Then for the GLRT of the replacement model, Figure 6.8 (f) shows that the GLRT using the refined orthogonal subspaces had poor performance compared to Figure 6.8 (e), where the original subspaces were applied for the GLRT.

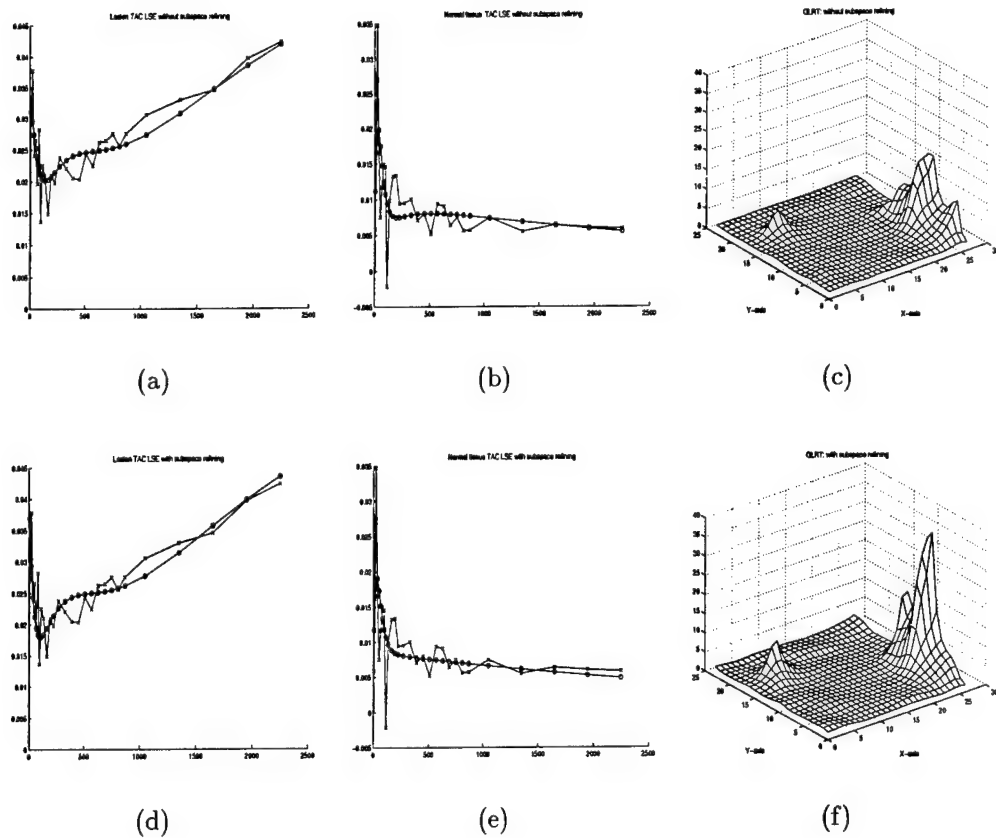


Figure 6.7: Subspace refining using the subspace distance measure. Without subspace refining: (a) lesion TAC and (b) normal tissue TAC both show the fidelity of subspaces estimated from observed TAC, (c) GLRT. With subspace refining: (d) lesion TAC and (e) normal tissue TAC shows the fidelity of subspace refined. It is clear that the refined subspaces maintain the fidelity requirement. (f) GLRT performance is improved by using the refined subspaces.

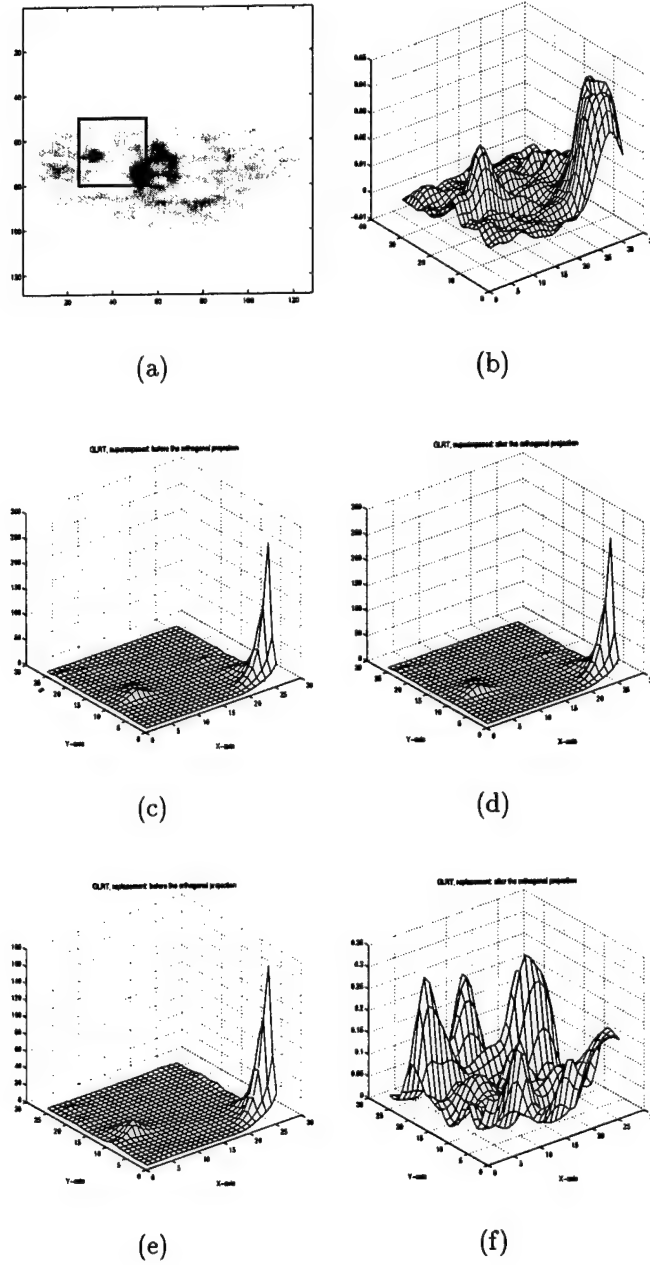


Figure 6.8: Subspace refining using the orthogonal projection. (a) test region inside the lung cancer image, (b) original 3D mesh. GLRT for the superimposed model: before, (c), and after, (d), the orthogonal subspace refining. GLRT for the replacement model: before, (e), and after, (f), the orthogonal subspace refining.

6.2.1.4 MAP Reconstructed Image

We also tested the GLRT for the lung cancer FGD-PET dynamic study by the MAP reconstructed algorithms [42, 18, 43, 24]. For the non-white noise case, the fast covariance calculation method proposed by Jinyi and Leahy [31] for the MAP image was used here for the decorrelation purpose. This covariance calculation method was summarized in Appendix B. We used the same subspaces estimated from the FBP image. The results of GLRT are shown in Figure 6.9.

6.2.2 Breast Cancer FDG-PET Dynamic Study

In this case, we examined a clinical, 36-frame, dynamic FDG-PET study of a patient with a primary breast cancer and a known axillary metastasis. The primary cancer was clearly visualized in the left breast, while the smaller axillary metastasis lymph node was marginally visualized, see Figure 6.10 (a)-(b). TACs obtained in the ROI placed on these tumors and contralateral normal breast tissue are shown in Figure 6.10 (c). The TACs showed that FDG radiotracer uptake within the lesions increases with time, while the TAC decreases for normal tissue.

The subspaces for the breast lesions and the normal tissues were identified using the SVD method. The subspace fidelity and separability were demonstrated by fitting the metastasis lymph node ROI onto the subspaces estimated from the primary

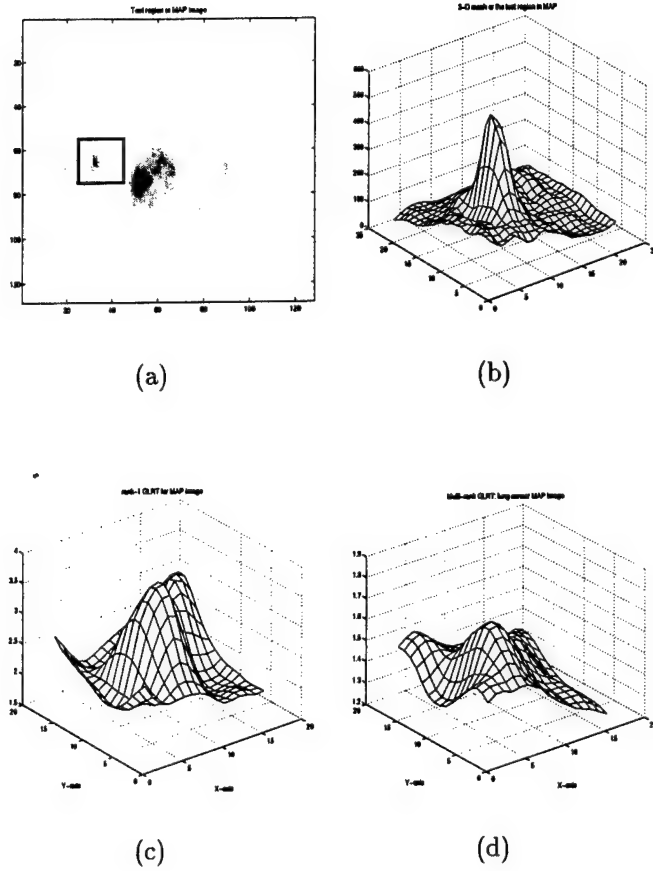


Figure 6.9: The MAP reconstructed lung cancer FDG-PET image. (a) The test region indicated by a rectangular for the GLRT. (b) 3-D mesh of the original test region. (c) GLRT: white Gaussian noise. (d) GLRT: non-white Gaussian noise.

cancer ROI and the normal breast tissue ROI. Figure 6.11 (d) shows that the subspace of the lesion TACs is approximately invariant between different tumors and the subspaces of the normal tissue and the lesion TACs were different. For a test region, right rectangle in Figure 6.11 (a), containing the small lesion, applications of the GLRT with replacement model showed that the lesion-to-normal tissue contrast was enhanced relative to the original FBP image, Figure 6.11 (f), while for a normal tissue test region, left rectangle in Figure 6.11 (a), the GLRT shows no enhancement.

An interesting GLRT result for this breast cancer dynamic study was the enhancement of an unknown lesion which could not be confirmed by eye. This unknown lesion was roughly located (confirmed by a later scan) inside the rectangular region shown in Figure 6.12 (a) and (b), but was undiscernible to human eyes even using a MAP reconstruction method. This patient did not have a follow-up scan until 18 months later. From the newly acquired data, the “new” lesion was confirmed. The results of GLRT (whit-noise assumption) based on the earlier FDG-PET scan of this patient showed that this unknown lesion was detected successfully in both MAP and FBP images, see Figure 6.12 (e) and (f), when compared to the 3-D mesh of the test region, see Figure 6.12 (c) and (d).

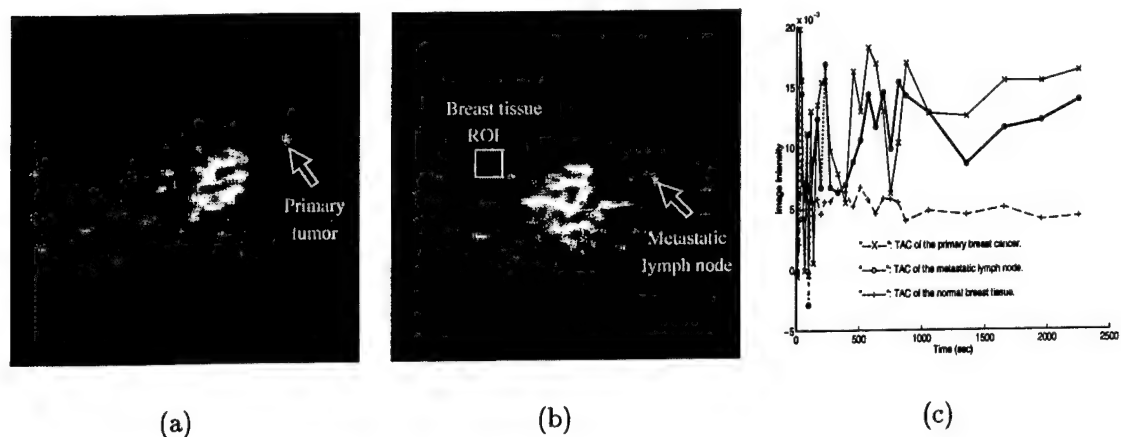


Figure 6.10: Breast cancer study: (a) a plane containing a primary cancer indicated by an arrow, (b) a plane containing a metastatic lymph node indicated by an arrow, (c) the TACs from the primary cancer, the metastatic lymph node and normal breast tissues in an ROI indicated with a rectangle in (b).

6.3 Phantom Dynamic Study

6.3.1 Computer Simulated Phantom Data

Two computer simulated phantoms, one with five artificial lesions at the known locations and the other with no lesions, were used in the phantom dynamic study, see Figure 6.13 (a)-(b). The TACs of the normal and malignant tissues measured from the clinical lung cancer FDG-PET dynamic study were applied to simulate the lesion and normal tissue kinetics behavior, see Figure 6.13 (c).

During the forward projection of the phantom dynamic image, the total count of projection data in each frame was scaled to approach the total count of the

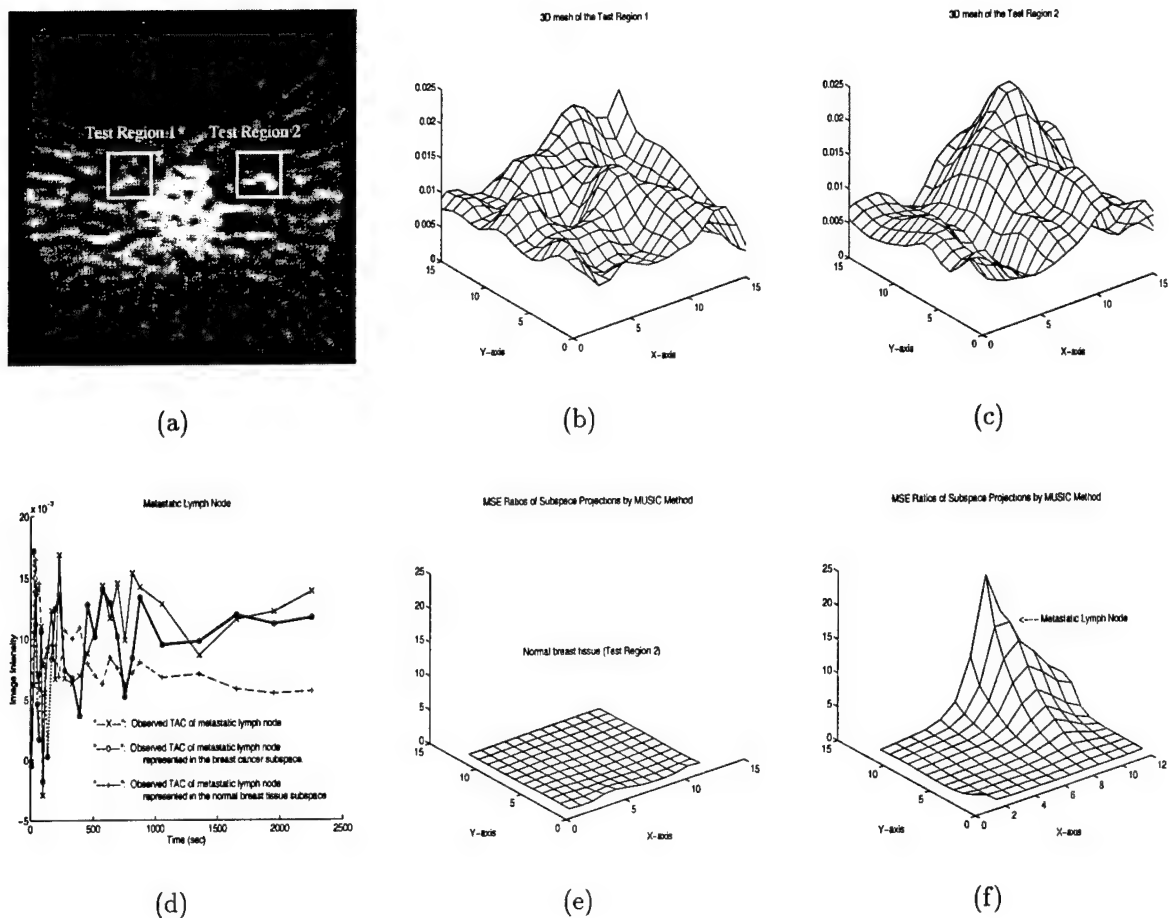


Figure 6.11: Breast cancer dynamic study: (a) two selected test regions: test region 1 containing the normal breast tissue and test region 2 containing a metastatic lymph node in the FBP image (same as (b)), (b)-(c) 3-D mesh of test region 1 and test region 2 indicated in (d). (d) TAC of the metastatic lymph node represented by the lesion subspace and normal breast tissue subspace identified by the SVD method, respectively, (e)-(f) the GLRT results on test region 1 and 2, respectively.

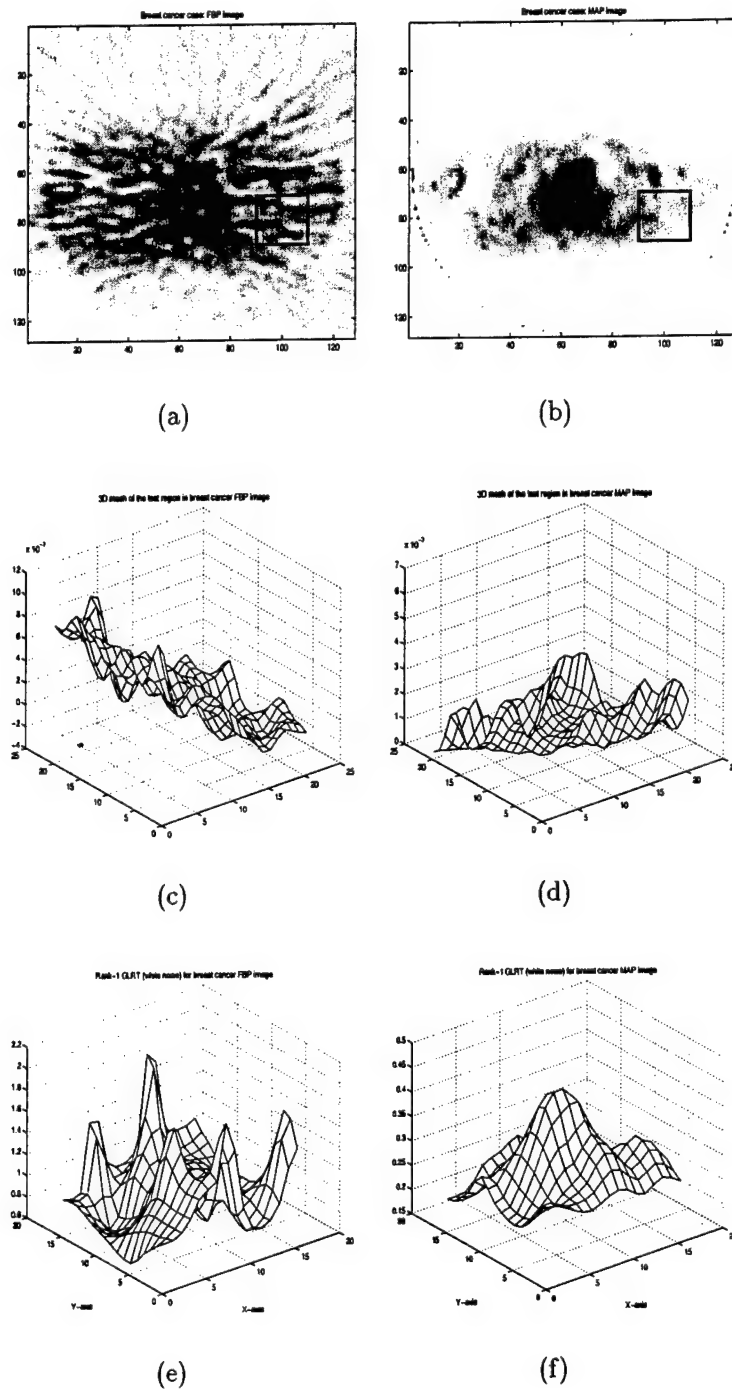


Figure 6.12: A GLRT result of enhancing an “unknown” lesion in the breast cancer FDG-PET dynamic study. The test region containing the unknown lesion in (a) FBP and (b) MAP. The 3-D mesh of the test region: (c) FBP and (d) MAP. GLRT (white noise): (e) FBP and (f) MAP.

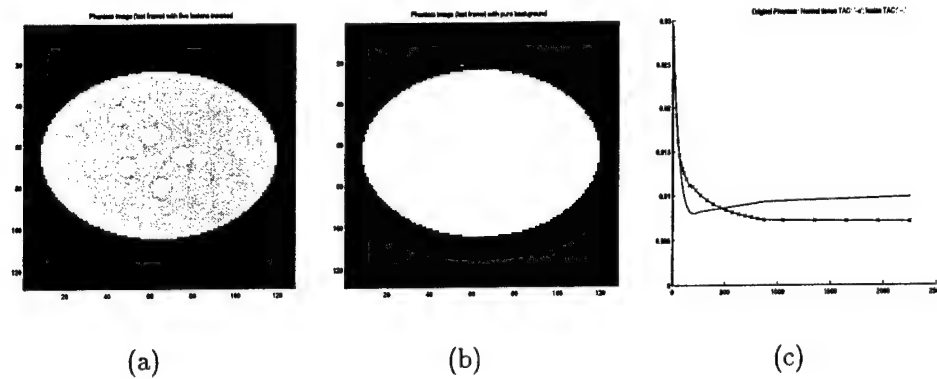


Figure 6.13: Left: lesion phantom image with 5 lesions, middle: normal tissue phantom with no lesions, right: TACs for lesion and normal tissues.

corresponding frame in a clinical dynamic study. This will be called the low count dynamic study in this research, while the total count of projection data for a high count study is twice of the total count in a clinical dynamic study. During the forward process, the sinogram data were corrupted with Poisson noise and blurred kernels to simulate the noise process and system resolution. FBP, MAP, and OSEM reconstruction methods were used for dynamic phantom image reconstruction. The images (last frame) reconstructed by the FBP, MAP, and OSEM methods and the corresponding observed TACs of normal and lesion tissues in the phantom dynamic images are presented in Figure 6.14, where the reconstructed lesion images looked like normal tissue images and the artificial lesions were hardly confirmed.

The GLRT results for the FBP dynamic images are shown in Figure 6.15 (high count data) and 6.16 (low count data), and the GLRTs for the MAP low count dynamic phantom images were shown in Figure 6.17. The GLRT results for both high count data and low count data improved the visualization of the artificial lesion locations.

6.3.2 Receiver Operating Characteristic (ROC) Study

An ROC study was applied to the phantom dynamic study for comparing the performance of detectors. Fifty lesion phantom studies (with 250 known lesions) and fifty normal tissue phantom dynamic studies were conducted in a Monte Carlo simulation. The rates of true and false positive decisions made from the three GLRT tests were counted, respectively. The ROC curves were estimated by using the software package *ROCKIT 0.9B* developed by Professor C.E. Metz, University of Chicago.

The resulting ROC curves from the FBP reconstructed dynamic phantom images shows that the GLRT with spatial decorrelation (with area under curve $A_z=0.92$) are close to that for the GLRT with a white-noise ($A_z=0.93$), see Figure 6.18 (a). The ROC curve from the multi-pixel GLRT further improved the A_z ($=0.98$).

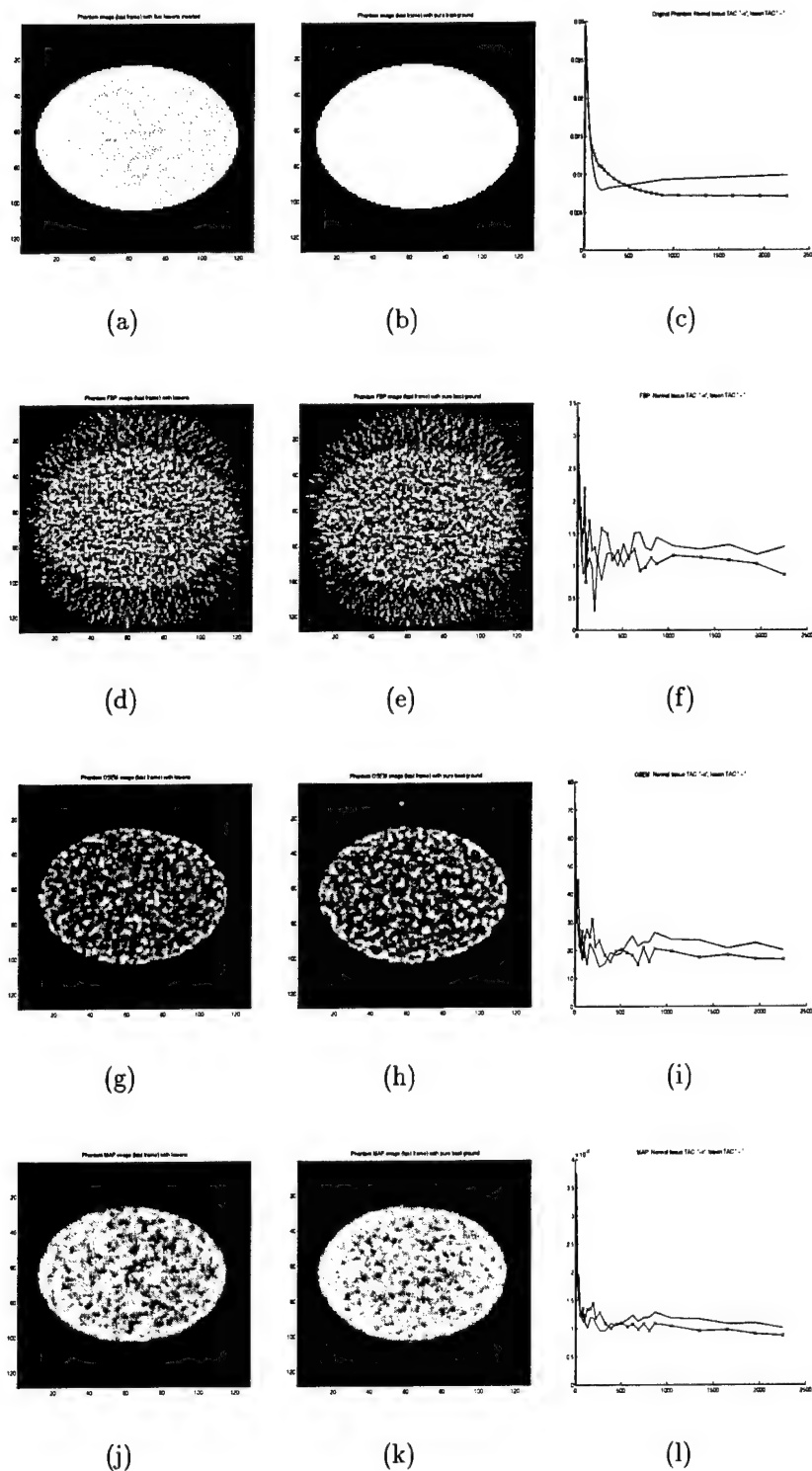
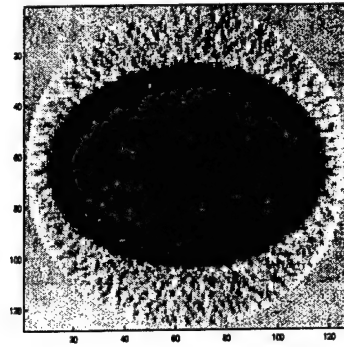
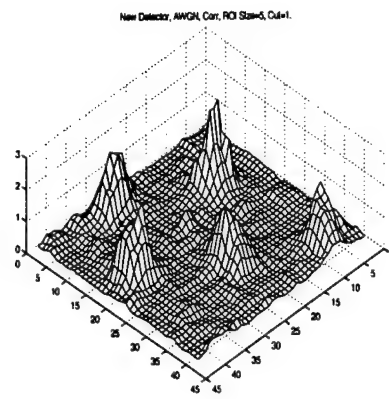


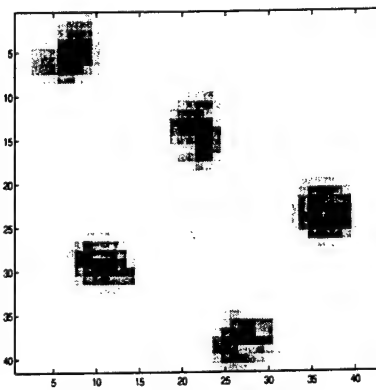
Figure 6.14: Left column: lesion phantom image with 5 lesions, middle column: normal tissue phantom with no lesions, right column: TACs for lesion and normal tissues. From top row to bottom: original phantom, FBP, OSEM, and MAP reconstructed images.



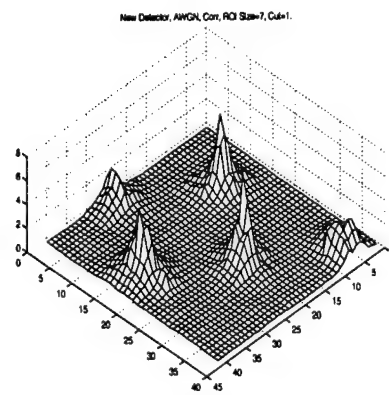
(a)



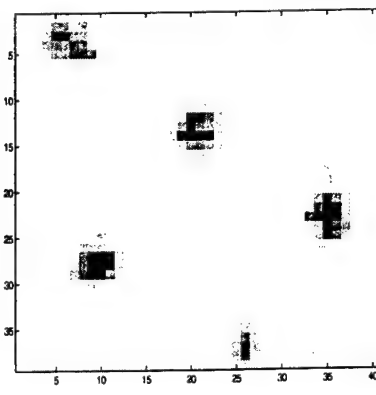
(b)



(c)

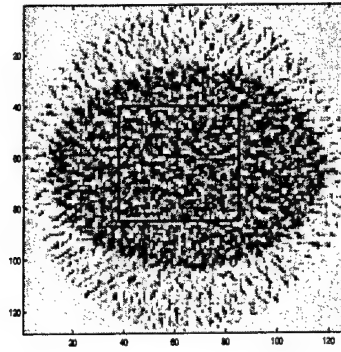


(d)

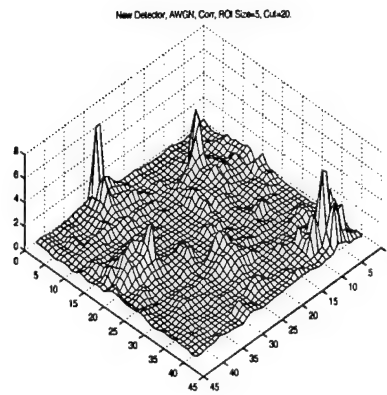


(e)

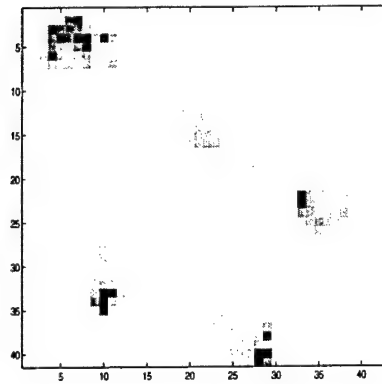
Figure 6.15: The GLRT for high count FBP phantom data: (a) a test region, (b)-(c) white noise assumption, (d)-(e) non-white noise assumption.



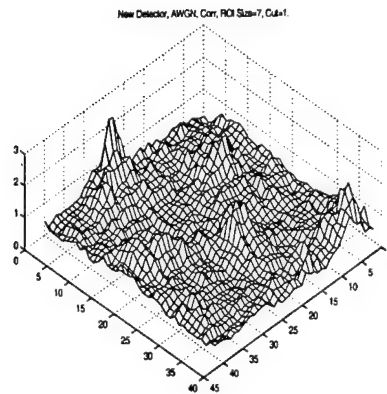
(a)



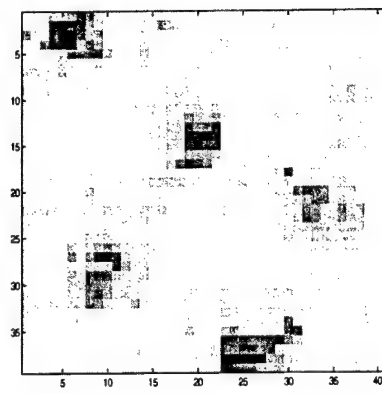
(b)



(c)



(d)



(e)

Figure 6.16: The GLRT for low count FBP data: (a) a test region, (b)-(c) white noise assumption, (d)-(e) non-white noise assumption.

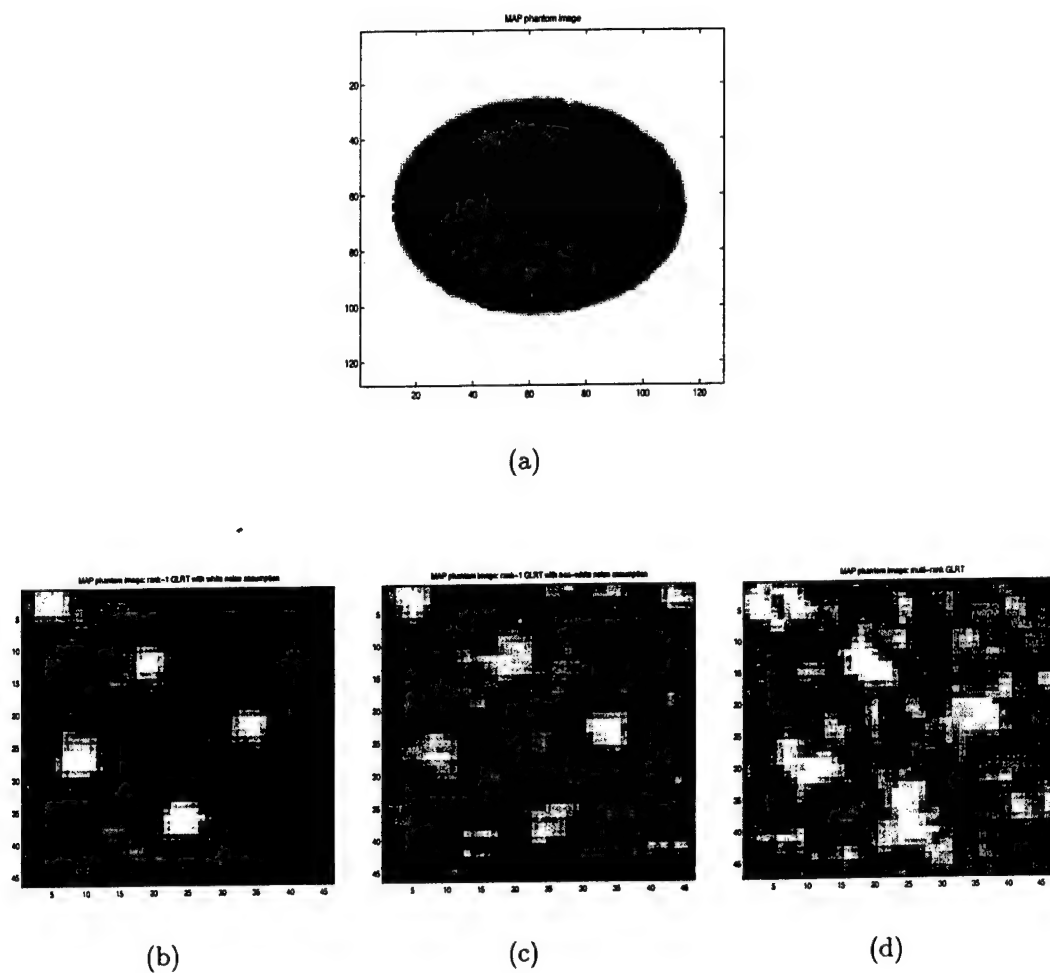


Figure 6.17: The GLRT for an MAP phantom image (low count data): (a) a test region indicated by a rectangular, (b): GLRT (white noise assumption), (c): GLRT (non-white noise assumption), (d): multi-pixel GLRT.

We also compared the GLRT performance for different reconstruction algorithms. The measured A_z for our ROC curves can be viewed as a computer observers for different reconstruction algorithms. A reconstruction algorithm can be claimed “better” if it achieves a higher A_z . Figure 6.18 (b) shows that the A_z (MAP) > A_z (OSEM) > A_z (FBP) which can be interpreted as the iterative reconstruction methods (MAP and OSEM) outperform the FBP method not only in image visualization, but also in the GLRT detection performance.

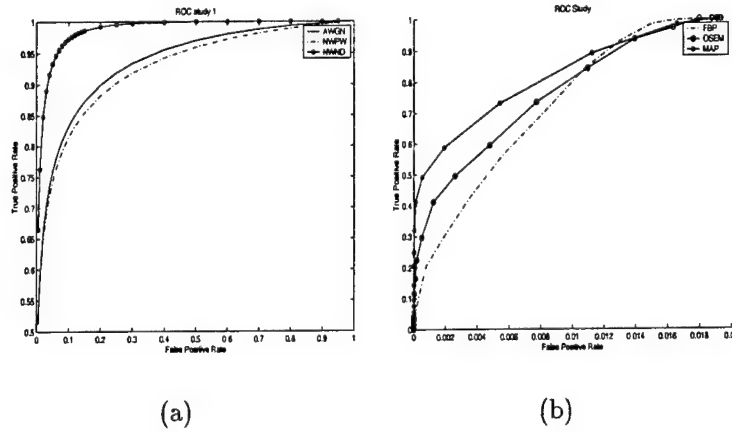


Figure 6.18: ROC curves for the low count data simulation: (a) FBP: GLRT (white noise, non-white noise) vs multi-pixel GLRT, where A_z (multi-pixel GLRT) > A_z (GLRT with non-white noise) $\approx A_z$ (GLRT with white noise). (b) GLRT with white noise assumption: A_z (MAP) > A_z (OSEM) > A_z (FBP).

Chapter 7

Conclusion

In order to improve early detection of small lesions using FDG-PET, computer-aided lesion detection algorithms have been developed in this dissertation to assist visual inspection in tumor detection using dynamic FDG-PET. In our approach, we hypothesized that the spatial and temporal metabolic features available from dynamic FDG-PET images are identifiable in a clinically practical way and useful for lesion detection. We showed that malignancies can be distinguished from normal tissues on the basis of their rates of FDG uptake in terms of time activity curves, given that lesions and normal tissues often differ in the rate of radiotracer accumulation or disappearance. Since the rates of FDG uptake in tissues are often characterized by a set of physiological factors and the time activity curves can be represented as a linear combination of the physiological factors, we used the subspace spanned by

the physiological factors as a key feature to distinguish normal tissues from malignancies. By forming the dynamic FDG-PET images into useful spatial-temporal data matrices, we were able to estimate the tumor and normal tissue subspaces by signal subspace fitting methods that are widely used in array signal processing. Then, applying the generalized maximum likelihood ratio principle, we adapted and generalized the matched subspace detection techniques for small lesion detection in dynamic FDG-PET. We demonstrated that with the matched subspace detectors, the subspace feature(s) extracted from visible, large lesions can be employed to confirm suspected, but not unequivocally identifiable, small lesions. Results from both clinical dynamic FDG-PET studies of patients with breast or lung cancer and dynamic phantom data showed that the physiological subspaces are straightforward to identify and distinct for known tumors and normal tissues, and are valuable for improving lesion diagnosis when combined with the matched subspace detection criteria. Therefore, the detection methods proposed in this dissertation are promising for improving early detection of small lesions. Based on these results, it is our belief that such detection methods can be used to reduce costly multiple diagnostic procedures and to guide surgical intervention.

Bibliography

- [1] L. P. Adler, J. P. Crowe, N. K. Al-kaisi, *et al.*, "Evaluation of breast masses and axillary lymph nodes with [F-18] 2-deoxy-2-fluoro-D-glucose PET," *Radiology*, 187, pp. 743-750, 1993.
- [2] J. Aliresaie, C. Nahmias, and M. E. Jernigan, "Neural network based segmentation of magnetic resonance images of the brain," *IEEE Nuclear Science Symposium*, 3, pp. 1397-1401, 1995.
- [3] N. M. Alpert, *et al.*, "Estimation of the local statistical noise in emission computed tomography," *IEEE Transactions on Medical Imaging*, vol. MI-1, no. 2, pp. 142-146, Oct. 1982.
- [4] S. C. Amartur, D. Piraino, and Y. Takefuji, "Optimization neural networks for the segmentation of magnetic resonance images," *IEEE Transactions on Medical Imaging*, vol. 11, no. 2, pp. 215-220, 1992.
- [5] D. Barber, "The use of principal components in the quantitative analysis of gamma camera dynamic studies," *Physics in Medicine and Biology*, 25, pp. 283-292, 1980.
- [6] R. T. Behrens and L. L. Scharf, "Signal processing applications of oblique projection operators," *IEEE Transactions on Signal Processing*, vol. 42, no. 6, pp. 1413-1424, June 1994.
- [7] R. E. Carson, *et al.*, "An approximation formula for the variance of PET region-of-interest values," *IEEE Transactions on Medical Imaging*, vol. 12, no. 2, pp. 240-250, June 1993.
- [8] S. R. Cherry and M. E. Phelps, "Imaging brain function with positron emission tomography," Chapter 8 in *Brain Mapping: The Methods*, edited by A. W. Toga and J. C. Mazziotta, Academic Press, 1996.
- [9] H. S. Choi, D. R. Haynor, and Y. Kim, "Partial volume tissue classification of multichannel magnetic resonance images - a mixed model," *IEEE Transactions on Medical Imaging*, vol. 10, no. 3, Sep. 1991.

- [10] P. S. Conti, *et al.*, "Carbon-11 labeled alpha-aminoisobutyric acid, 2-deoxy-D-glucose, and thymidine as potential imaging agents for prostatic and renal malignancies," *Surgical Forum*, vol. 36, pp. 635-637, 1985.
- [11] P. S. Conti, *et al.*, "Multiple radiotracers for evaluation of intracranial mass lesion using PET," *Journal of Nuclear Medicine*, vol. 32, pp. 954-970, 1991.
- [12] P. S. Conti, *et al.*, "PET and [^{18}F]-FDG in oncology: a clinical update," *Nuclear Medicine and Biology*, vol. 23, pp. 717-735, 1996.
- [13] T. M. Cover, "An algorithm for maximizing expected log investment return," *IEEE Transactions on Information Theory*, vol. IT-30, no. 2, pp. 369-373, Mar. 1984.
- [14] L. P. Crowe, L. P. Adler, R. R. Shenk, and J. Sunshine, "Positron emission tomography and breast masses: comparison with clinical, mammographic, and pathological findings," *Annals Surgical Oncology*, vol. 1, pp. 132-140, 1994.
- [15] V. J. Cunningham and T. Jones, "Spectral analysis of dynamic PET studies," *Journal of Cerebral Blood Flow and Metabolism*, 13, 15-23, 1993.
- [16] D. Feng and X. Wang, "A computer simulation study on the effects of input function measurement noise in tracer kinetic modeling with positron emission tomography (PET)," *Computer Biology Medicine*, vol. 23, no. 1, pp. 57-68, 1993.
- [17] R. H. Huesman, "A new fast algorithm for the evaluation of regions of interest and statistical uncertainty in computed tomography," *Physics in Medicine and Biology*, vol. 29, no. 5, pp. 543-552, 1984.
- [18] E. Ü. Mumcuoğlu, R. M. Leahy, S. R. Cherry, and Z. Zhou, "Fast gradient-based methods for Bayesian reconstruction of transmission and emission PET images," *IEEE Transactions on Medical Imaging*, vol. 13, no. 4, pp. 687-701, Dec. 1994.
- [19] J. A. Fessler, "Mean and variance of implicitly defined biased estimators (such as penalized maximum likelihood): application to tomography," *IEEE Transactions on Image Processing*, vol. 5, no. 3, pp. 493-506, Mar. 1996.
- [20] J. A. Fessler, "Approximate variance images for penalized-likelihood image reconstruction," *IEEE Nuclear Science Symposium and Medical Imaging Conference*, Albuquerque, NM, 1997.
- [21] G. H. Golub and C. F. Van Loan, *Matrix Computation*, 3rd edition, the Johns Hopkins University Press, 1996.

- [22] G. L. Brownell, T. F. Budinger, P. C. Lauterbur, and P. L. McGeer, "Positron tomography and nuclear magnetic resonance imaging," *Science*, pp. 619-626, Feb. 1982.
- [23] P. J. Green, "Bayesian reconstruction from emission tomography data using a modified EM algorithm," *IEEE Transactions on Medical Imaging*, vol. MI-9, no. 1, pp. 84-93, Mar. 1990.
- [24] T. J. Hebert and R. M. Leahy, "A generalized EM algorithm for 3-D Bayesian reconstruction from Poisson data using Gibbs priors," *IEEE Transactions on Medical Imaging*, vol. MI-8, no. 2, pp. 194-202, June 1989.
- [25] H. M. Hudson and R. S. Larkin, "Accelerated image reconstruction using ordered subsets of projection data," *IEEE Transactions on Medical Imaging*, 1994.
- [26] C. C. Huang and X. Yu, "Computer-aided lesion detection with statistical model-based features in PET images," *USC-Radiology Internal Report*, July 1996.
- [27] C. C. Huang, X. Yu, J. Zheng, J. R. Bading, and P. S. Conti, "Algorithm to reduce the complexity of local statistics computation for PET images," *SPIE Proceedings on Medical Imaging*, vol. 3034, pp. 1094-1111, Newport Beach, CA, Feb. 1997.
- [28] C. C. Huang, X. Yu, J. R. Bading, and P. S. Conti, "Computer-aided lesion detection with statistical model-based features in PET images," *IEEE Transactions on Nuclear Science*, vol. 44, no. 6, pp. 2509-2521, Dec. 1997.
- [29] C. C. Huang, X. Yu, J. Bading, and P. S. Conti, "Feature extraction by subspace fitting of time activity curve in PET dynamic studies," *IEEE Nuclear Science Symposium and Medical Imaging Conference*, Albuquerque, NM, Nov. 1997.
- [30] R. H. Huesman, "A new fast algorithm for the evaluation of regions of interest and statistical uncertainty in computed tomography," *Physics in Medicine and Biology*, vol. 29, No 5, pp. 543-552, 1984.
- [31] J. Qi and R. M. Leahy, "Fast computation of the covariance of MAP reconstructions of PET images," *Proceedings of SPIE*, San Diego, CA, 1999.
- [32] A. C. Kak and M. Slaney, *Principles of Computerized Tomography Imaging*, IEEE Press, 1987.
- [33] K. Kubota, T. Matsuzawa, *et al.*, "Differential diagnosis of lung tumor with positron emission tomography: a prospective study," *Journal of Nuclear Medicine*, vol. 31, pp. 1927-1933, 1990.

- [34] J. Llacer, *et al.*, "Results of a clinical receiver operating characteristic study comparing filtered backprojection and maximum likelihood estimator images in FDG PET studies," *Journal of Nuclear Medicine*, vol. 34, pp. 1198-1203, 1993.
- [35] G. Lucignani, K. C. Schmidt, R. M. Moreco, *et al.*, "Measurement of regional cerebral glucose utilization with fluorine-18-FDG and PET in heterogeneous tissues: theoretical considerations and practical procedures," *Journal of Nuclear Medicine*, vol. 34, No. 3, 360-369, Mar. 1993.
- [36] S. R. Meikle and M. Dahlbom, "Positron emission tomography: application in oncology," in *Nuclear Medicine in Clinical Diagnosis and Treatment*, edited by I. P. C. Murray and P. J. Ell, vol. 2, pp. 1327-1337.
- [37] S. R. Meikle, J. C. Matthews, V. J. Cunningham, *et al.*, "Spectral analysis of PET projection data," *IEEE Nuclear Science Symposium and Medical Imaging Conference*, p. 1888-1892, 1997.
- [38] C. E. Metz, "Basic principles of ROC analysis," *Seminars in Nuclear Medicine*, vol. 4, pp. 283-298, 1978.
- [39] M. M. Ter-Pogossian, M. E. Raichle, and B. E. Sobel, "Positron emission tomography," *Scientific American*, 243 (4), pp. 171-181, 1980.
- [40] J. C. Mosher, P. S. Lewis, and R. M. Leahy, "Multiple dipole modeling and localization from spatio-temporal MEG data," *IEEE Transactions on Biomedical Engineering*, vol. 39, no. 6, pp. 541-557, June 1992.
- [41] J. C. Mosher and R. M. Leahy, "Recursive MUSIC: a framework for EEG and MEG source localization," *IEEE Transactions on Biomedical Engineering*, vol. 45, no. 11, pp. 1342-1354, Nov. 1998.
- [42] E. Ü. Mumcuoğlu, R. M. Leahy, and S. R. Cherry, "Bayesian reconstruction of PET images: quantitative methodology and performance analysis," *Journal of Computer Assisted Tomography*, Jan. 1994.
- [43] E. Ü. Mumcuoğlu, R. M. Leahy, and S. R. Cherry, "Bayesian reconstruction of PET images: methodology and performance analysis," *Physics in Medicine and Biology*, vol. 41, no. 9, pp. 1777-1807, Sep. 1996.
- [44] K. S. Nijran and D. Barber, "Towards automatic analysis of dynamic radionuclide studies using principal-component factor analysis," *Physics in Medicine and Biology*, 30, pp. 1315-1325, Dec. 1985.
- [45] K. S. Nijran and D. Barber, "Factor analysis of dynamic function studies using a priori physiological information," *Physics in Medicine and Biology*, 31, pp. 1107-1117, Oct. 1986.

- [46] D. Ortendahl, "The application of principal component analysis to multivariate MRI data," *Proceedings of the 8th Annual Conference of the Engineering in Medical and Biology Society*, p. 1065-1068, Fort Worth, TX, 1986.
- [47] F. O'Sullivan, "Imaging radiotracer model parameters in PET: a mixture analysis approach," *IEEE Transactions Medical Imaging*, vol. 12, no. 3, pp. 399-412, 1993.
- [48] R. Maitra and F. O'Sullivan, "Estimating the variability of reconstructed PET data: a technique based on approximating the reconstruction filter by a sum of Gaussian kernels," *IEEE Nuclear Science Symposium and Medical Imaging Conference*, vol. 3, pp. 1411-1414, 1995.
- [49] F. Pedersen, M. Bergstrom, E. Bengtsson, and B. Langstrom, "Principal component analysis of dynamic positron emission tomography images," *European Journal of Nuclear Medicine*, vol. 21, no. 12, pp. 1285-1292, Dec. 1994.
- [50] M. E. Phelps, J. C. Mazziotta, and H. R. Schelbert, *Positron Emission Tomography and Autoradiology, Principles and Applications for the Brain and Heart*, Raven Press, 1986.
- [51] I. S. Reed and X. Yu, "Adaptive multi-band CFAR detection of an optical pattern with unknown spectral distribution," *IEEE Transactions on Acoustic, Speech, and Signal Processing*, vol. 38, no. 10, Oct. 1990.
- [52] L. E. Brennan and S. Reed, "A digital adaptive antenna for JTIDS," submitted to the Electronic Systems Division, AFSC, USAF, Hanscom AFB, MA 01731, Dec. 6, 1989.
- [53] P. Santago, and H. D. Gage, "Quantification of MR brain images by mixture density and partial volume modeling," *IEEE Transactions on Medical Imaging*, vol. 12, no. 3, Sep. 1993.
- [54] L. L. Scharf, *Statistical Signal Processing*, MA: Addison-Wesley, 1991.
- [55] L. L. Scharf and B. Friedlander, "Matched subspace detectors," *IEEE Transactions on Signal Processing*, vol. 42, no. 8, pp. 2146-2157, Aug. 1994.
- [56] B. Schmall, P. S. Conti, D. J. Schaeffer, and E. L. Kleinert, "Tumor and organ biochemical profiles determined in vivo following uptake of a combination of radiolabeled substrates: potential applications for PET," *American Journal of Physics Imaging*, vol. 7, pp. 2-11, 1992.
- [57] K. Schmidt, G. Mies, and L. Sokoloff, "Model of kinetic behavior of deoxyglucose in heterogeneous tissues in brain: a reinterpretation of the significant of parameters fitted to homogeneous tissue models," *Journal of Cerebral Blood Flow and Metabolism*, vol. 11, pp. 10-24, 1991.

- [58] S. C. Huang, M. E. Phelps, E. J. Hoffman, K. Sideris, C. J. Selin, and D. E. Kuhl, "Noninvasive determination of local cerebral metabolic rate of glucose in man," *American Journal of Physiology*, E69-E82, 1980.
- [59] L. A. Shepp and B. F. Logan, "The Fourier reconstruction of a head section," *IEEE Transactions on Nuclear Science*, NS-21, pp. 21-43, June 1974.
- [60] L. A. Shepp and Y. Vardi, "Maximum likelihood reconstruction for emission tomography," *IEEE Transactions on Medical Imaging*, MI-1, no. 2, pp. 113-122, Oct. 1982.
- [61] Z. H. Cho, J. Jones, and M. Singh, *Foundations of Medical Imaging*, John Wiley & Sons, Inc., New York, 1993.
- [62] L. G. Strauss and P. S. Conti, "The applications of PET in clinical oncology," *Journal of Nuclear Medicine*, vol. 32, no. 4, pp. 623-648, Apr. 1991.
- [63] T. X-L Tan, M. Y. Klein, V. T. Tabib, C. Turner, and J. M. Forde, "Oncology applications of PET: an updated review," *Applied Radiology*, p. 18-25, June 2000.
- [64] E. Tanaka and H. Murayama, "Properties of statistical noise in positron emission tomography," *IEEE Proceedings of International Workshop Physics Engineering Medical Imaging*, p. 158-164, New York, 1982.
- [65] G. D. Tourassi and C. E. Floyd, "Artificial neural networks for single photon emission computed tomography: a study of cold lesion detection and location," *Investigative Radiology*, vol. 28, no. 8, pp. 671-677, Aug. 1993.
- [66] F. Turkheimer, R. M. Moresco, G. Lucignani, *et al.*, "The use of spectral analysis to determine regional cerebral glucose utilization with positron emission tomography and [^{18}F]-fluorodeoxyglucose: theory, implementation, and optimization procedures," *Journal of Cerebral Blood Flow and Metabolism*, 14, 406-422, 1994.
- [67] Let's Play PET, <http://www.crump.ucla.edu/lpp>.
- [68] Y. Vardi, L. A. Shepp, and L. Kaufman, "A statistical model for positron emission tomography," *Journal of American Association*, vol. 80, no. 389, 8-20, Mar. 1985.
- [69] M. Viberg and B. Ottersten, "Sensor array processing based on subspace fitting," *IEEE Transactions on Signal Processing*, vol. 39, no. 5, pp. 1110-1121, May 1991.

- [70] R. L. Wahl, "Positron emission tomography: application in oncology," in *Nuclear Medicine in Clinical Diagnosis and Treatment*, edited by I. P. C. Murray and P. J. Ell, vol. 2, pp. 801-820.
- [71] R. L. Wahl, G. D. Hutchins, D. J. Buchsbaum, M. Liebert, H. B. Grossman, and S. Fisher, "¹⁸F-2-deoxy-2-fluoro-D-glucose uptake into human tumor xenografts: feasibility studies for cancer imaging with positron-emission tomography," *Cancer*, vol. 67, pp. 1544-1550, 1991.
- [72] R. L. Wahl, R. Cody, G. D. Hutchins, and E. Mudgett, "Primary and metastatic breast carcinoma: initial clinical evaluation with PET with the radiolabeled glucose analog 2-[F-18]-fluorodeoxy-2-D-glucose(FDG)," *Radiology*, vol. 179, pp. 765-770, 1991.
- [73] D. W. Wilson and M. W. Benjamin, "Noise properties of filtered-backprojection and ML-EM reconstructed emission tomographic images," *IEEE Transactions on Nuclear Medicine*, vol. 40, no. 4, pp. 1198-1203, Aug. 1993.
- [74] X. Yu, I. S. Reed, and A. Stocker, "Performance comparison of adaptive multi-band optical target detection," *IEEE Transactions on Signal Processing*, Aug. 1993.
- [75] X. Yu, *et al.*, "A linear feature mapping framework for adaptive detection and recognition of targets in complex SAR data," *IEEE 28th Conference on Signal, System, and Computers*, Monterey, CA, Oct. 30-Nov. 2, 1994.
- [76] X. Yu, J. R. Bading, and P. S. Conti, "Automated lesion detection with feature analysis in positron emission tomography," *IEEE Nuclear Science Symposium and Medical Imaging Conference*, Norfolk, VA, Nov. 3-6, 1994.
- [77] X. Yu, A. M. Chen, and I. S. Reed, "A maximum likelihood detection of signals using feature mapping framework," *Proceedings of IEEE ICASSP*, Detroit, MI, May 1995.
- [78] X. Yu and I. S. Reed, "Adaptive detection of signals with linear feature mappings and representations," *IEEE Transactions on Signal Processing*, vol. 43, no. 12, Dec. 1995.
- [79] X. Yu, C. C. Huang, R. M. Leahy, J. R. Bading, and P. S. Conti, "Analytic computation and sample estimation of the local statistics of positron emission tomography images: a comparative study," *Proceedings of the 43rd Annual Meeting of the Society of Nuclear Medicine*, Denver, CO, June 3-5, 1996.
- [80] X. Yu and C. C. Huang, "Lesion detection with statistical model-based prior information in positron emission tomography," *IEEE Nuclear Science Symposium and Medical Imaging Conference*, Anaheim, CA, Nov. 2-9, 1996.

- [81] X. Yu, L. E. Hoff, I. S. Reed, *et al.*, "Automated target detection and recognition in multi-band imagery: a unified ML detection and estimation approach," *IEEE Transactions on Image Processing*, vol. 6, no. 1, pp. 134-156, Jan. 1997.
- [82] X. Yu, C. C. Huang, J. R. Bading, and P. S. Conti, "Use of a matched subspace filter for lesion detection in dynamic positron emission tomography," *Annual Meeting of Society of Nuclear Medicine*, San Antonio, TX, June 2-5, 1997.

Appendix A

Oblique Projection

Let $\langle \mathbf{H} \rangle$ denote the subspace spanned by the matrix \mathbf{H} . If the subspaces $\langle \mathbf{H} \rangle$ (p -dimension) and $\langle \mathbf{S} \rangle$ (t -dimension) are linearly independent, then the columns of the concatenated matrix $[\mathbf{HS}]$ span a $(p + t)$ -dimensional subspace $\langle \mathbf{HS} \rangle$. The typical orthogonal projection of a TAC \mathbf{y} ($\in \mathcal{R}^N$) onto $\langle \mathbf{HS} \rangle$ is denoted by $\mathbf{P}_{HS}\mathbf{y}$, where \mathbf{P}_{HS} is the orthogonal projection in the subspace $\langle \mathbf{HS} \rangle$ and represented as

$$\mathbf{P}_{HS} = [\mathbf{HS}] \left([\mathbf{HS}]^T [\mathbf{HS}] \right)^{-1} [\mathbf{HS}]^T. \quad (\text{A.1})$$

We can further re-express \mathbf{P}_{HS} as

$$\begin{aligned} \mathbf{P}_{HS} &= \begin{bmatrix} \mathbf{H} & \mathbf{S} \end{bmatrix} \begin{bmatrix} \mathbf{H}^T \mathbf{H} & \mathbf{H}^T \mathbf{S} \\ \mathbf{S}^T \mathbf{H} & \mathbf{S}^T \mathbf{S} \end{bmatrix}^{-1} \begin{bmatrix} \mathbf{H}^T \\ \mathbf{S}^T \end{bmatrix} \\ &= \begin{bmatrix} \mathbf{H} & \mathbf{0} \end{bmatrix} \begin{bmatrix} \mathbf{H}^T \mathbf{H} & \mathbf{H}^T \mathbf{S} \\ \mathbf{S}^T \mathbf{H} & \mathbf{S}^T \mathbf{S} \end{bmatrix}^{-1} \begin{bmatrix} \mathbf{H}^T \\ \mathbf{S}^T \end{bmatrix} \\ &\quad + \begin{bmatrix} \mathbf{0} & \mathbf{S} \end{bmatrix} \begin{bmatrix} \mathbf{H}^T \mathbf{H} & \mathbf{H}^T \mathbf{S} \\ \mathbf{S}^T \mathbf{H} & \mathbf{S}^T \mathbf{S} \end{bmatrix}^{-1} \begin{bmatrix} \mathbf{H}^T \\ \mathbf{S}^T \end{bmatrix} \end{aligned}$$

$$\triangleq \mathbf{E}_{HS} + \mathbf{E}_{SH} \quad (\text{A.2})$$

where

$$\begin{aligned} \mathbf{E}_{HS} &\triangleq \begin{bmatrix} \mathbf{H} & \mathbf{0} \end{bmatrix} \begin{bmatrix} \mathbf{H}^T \mathbf{H} & \mathbf{H}^T \mathbf{S} \\ \mathbf{S}^T \mathbf{H} & \mathbf{S}^T \mathbf{S} \end{bmatrix}^{-1} \begin{bmatrix} \mathbf{H}^T \\ \mathbf{S}^T \end{bmatrix} \\ \mathbf{E}_{SH} &\triangleq \begin{bmatrix} \mathbf{0} & \mathbf{S} \end{bmatrix} \begin{bmatrix} \mathbf{H}^T \mathbf{H} & \mathbf{H}^T \mathbf{S} \\ \mathbf{S}^T \mathbf{H} & \mathbf{S}^T \mathbf{S} \end{bmatrix}^{-1} \begin{bmatrix} \mathbf{H}^T \\ \mathbf{S}^T \end{bmatrix}. \end{aligned}$$

The two projections, \mathbf{E}_{HS} and \mathbf{E}_{SH} , are called the *oblique* projections [6] with the property that \mathbf{E}_{HS} and \mathbf{E}_{SH} have respective range spaces $\langle \mathbf{H} \rangle$ and $\langle \mathbf{S} \rangle$ and respective null spaces $\langle \mathbf{S} \rangle$ and $\langle \mathbf{H} \rangle$, i.e.,

$$\begin{aligned} \mathbf{E}_{HS} \mathbf{H} &= \mathbf{H}, \quad \mathbf{E}_{HS} \mathbf{S} = \mathbf{0}, \\ \mathbf{E}_{SH} \mathbf{S} &= \mathbf{S}, \quad \mathbf{E}_{SH} \mathbf{H} = \mathbf{0}. \end{aligned} \quad (\text{A.3})$$

The simplification version of the *oblique* projections \mathbf{E}_{HS} and \mathbf{E}_{SH} can be written as

$$\begin{aligned} \mathbf{E}_{HS} &= \mathbf{H}(\mathbf{H}^T \mathbf{P}_S^\perp \mathbf{H})^{-1} \mathbf{H}^T \mathbf{P}_S^\perp \\ \mathbf{E}_{SH} &= \mathbf{S}(\mathbf{S}^T \mathbf{P}_H^\perp \mathbf{S})^{-1} \mathbf{S}^T \mathbf{P}_H^\perp. \end{aligned} \quad (\text{A.4})$$

Hence,

$$\begin{aligned}\mathbf{P}_{HS} &= \mathbf{E}_{HS} + \mathbf{E}_{SH} \\ &= \mathbf{H}(\mathbf{H}^T \mathbf{P}_S^\perp \mathbf{H})^{-1} \mathbf{H}^T \mathbf{P}_S^\perp + \mathbf{S}(\mathbf{S}^T \mathbf{P}_H^\perp \mathbf{S})^{-1} \mathbf{S}^T \mathbf{P}_H^\perp.\end{aligned}\tag{A.5}$$

Appendix B

Local Statistics in PET Images

B.1 Local Statistics Calculation in PET FBP images

The analytic computation (AC) for the local statistics of a PET FBP image was originally developed by Huesman [17]. By the independence of observation data and the linear properties of FBP, AC estimates the (co)variance of PET image pixels from the projection data statistics via some scaling factors. Huesman's algorithm calculates local statistics directly from the projection data without image reconstruction. Recently, Carson *et al.* [7] developed an approximation formula for the variance of PET ROI values, which accounted the radioactivity distribution, attenuation, random, scatter, deadtime, detector normalization, scan length, decay, and reconstruction filter. By the assumption that the pixel variances of any two pixels are similar, and that the product of attenuation, normalization, wobbling and raw

data is relatively uniform for those projection lines that substantially contribute to the sum, they derived a simple formula for the correlation coefficient of any two pixels, which is independent of the raw data.

Let the raw projection data in PET be an l -dimensional column vector $\mathbf{p} = [\mathbf{p}_1^T, \mathbf{p}_2^T, \dots, \mathbf{p}_{n_\theta}^T]^T$, where l is the product of the total number of angles (n_θ) and the total number of rays n_r , and \mathbf{p}_θ (size: $n_r \times 1$) is the sinogram data in the angle θ . Let the corrected data of \mathbf{p} be \mathbf{p}' which consists of

$$p'_{\theta,r} = A_{\theta,r}(N_{\theta,r}(W_r \cdot p_{\theta,r} - R_{\theta,r}) - S_{\theta,r}), \quad \theta = 1, 2, \dots, n_\theta, \quad r = 1, 2, \dots, n_r. \quad (\text{B.1})$$

The terms $A_{\theta,r}$ and $N_{\theta,r}$ in Eq. (B.1) are multiplicative correction terms for attenuation and detector efficiency (normalization). W_r corrects for the fraction of time spent in each wobble position and is generally independent of angle. $R_{\theta,r}$ and $S_{\theta,r}$ are the estimates of random and scatter. The terms $p_{\theta,r}$, $p'_{\theta,r}$, $R_{\theta,r}$, and $S_{\theta,r}$ have units of counts, while all other terms are dimensionless.

Therefore, for any pixel g_i with index i at position x_i, y_i , the pixel value calculated by the FBP is the convolution of the corrected projection data $p'_{\theta,r}$ with the reconstruction filter h , that is,

$$g_i = \sum_{\theta=1}^{n_\theta} \sum_{r=1}^{n_r} h(x_i \cos \theta + y_i \sin \theta - r) p'_{\theta,r}. \quad (\text{B.2})$$

In practice, additional linear interpolation steps are applied and the reconstructed pixel value becomes

$$g_i = \sum_{\theta=1}^{n_\theta} \sum_{r=1}^{n_r} h_{\theta,r}^{(i)} p'_{\theta,r} \quad (\text{B.3})$$

where $h_{\theta,r}^{(i)}$ is unique for the pixel i in FBP at angle θ and ray r .

B.1.1 Variance of Pixel in an ROI

From Eq. (B.3), the variance of the pixel i can be simply written as

$$\text{Var}\{g_i\} = \sum_{\theta=1}^{n_\theta} \sum_{r=1}^{n_r} \left(h_{\theta,r}^{(i)}\right)^2 \cdot \text{Var}\{p'_{\theta,r}\}. \quad (\text{B.4})$$

In a PET system, it is usually assumed that the significant source of noise in $p'_{\theta,r}$ is due to the Poisson statistics in the raw projection data $p_{\theta,r}$, that is, the noise in the term $A_{\theta,r}$, $N_{\theta,r}$, W_r , $R_{\theta,r}$, and $S_{\theta,r}$ is small. Also, the raw count $p_{\theta,r}$ are statistically independent Poisson distribution, so are the $p'_{\theta,r}$ by the Eq. (B.1). Therefore, the pixel variance in Eq. (B.4) can be approximated as

$$\begin{aligned} \text{Var}\{g_i\} &\cong \sum_{\theta=1}^{n_\theta} \sum_{r=1}^{n_r} \left(h_{\theta,r}^{(i)}\right)^2 \cdot \left[A_{\theta,r}^2 N_{\theta,r}^2 W_r^2\right] \cdot \text{Var}(p_{\theta,r}) \\ &\cong \sum_{\theta=1}^{n_\theta} \sum_{r=1}^{n_r} \left(h_{\theta,r}^{(i)}\right)^2 \cdot \left[A_{\theta,r}^2 N_{\theta,r}^2 W_r^2\right] \cdot p_{\theta,r}. \end{aligned} \quad (\text{B.5})$$

We can further assume that for each angle θ , the product of $p_{\theta,r}$ and $[A_{\theta,r}^2 N_{\theta,r}^2 W_r^2]$ is relatively uniform in the ROI, i.e., we can approximate $[A_{\theta,r}^2 N_{\theta,r}^2 W_r^2] p_{\theta,r}$ by some representative of them, namely $[A_{\theta}^2 N_{\theta}^2 W^2] p_{\theta}$. Therefore, Eq. (B.5) becomes

$$\begin{aligned}
\text{Var}(g_i) &\cong \sum_{\theta=1}^{n_{\theta}} \sum_{r=1}^{n_r} \left(h_{\theta,r}^{(i)}\right)^2 \cdot [A_{\theta}^2 N_{\theta}^2 W^2] p_{\theta} \\
&= \sum_{\theta=1}^{n_{\theta}} [A_{\theta}^2 N_{\theta}^2 W^2] p_{\theta} \cdot \sum_{r=1}^{n_r} \left(h_{\theta,r}^{(i)}\right)^2 \\
&= \sum_{\theta=1}^{n_{\theta}} [A_{\theta}^2 N_{\theta}^2 W^2] p_{\theta} \cdot \|\mathbf{h}_{\theta}\|_2^2 \\
&\cong \|\mathbf{h}\|_2^2 \cdot \sum_{\theta=1}^{n_{\theta}} [A_{\theta}^2 N_{\theta}^2 W^2] p_{\theta} \\
&= c_1 \cdot \sum_{\theta=1}^{n_{\theta}} [A_{\theta}^2 N_{\theta}^2 W^2] p_{\theta}
\end{aligned} \tag{B.6}$$

where $\|\mathbf{h}\|_2$ is defined as the 2-norm of the filter vector \mathbf{h} and \mathbf{h}_{θ} is the filter vector associated with the angle θ . We used the observation that the 2-norm of the filter vector \mathbf{h}_{θ} in all angle are approximately equal in an ROI, that is, $\|\mathbf{h}\|_2 \approx \|\mathbf{h}_{\theta}\|_2$, for all θ . Hence, the value $c_1 \triangleq \|\mathbf{h}\|_2^2$ can be determined *a priori* for the convolution filter used in the FBP.

B.1.2 Covariance of Pixels in an ROI

Following the similar steps in deriving the variance of a pixel, the covariance of any two pixels can be computed as

$$\begin{aligned} \text{Cov}(g_j, g_k) &= \sum_{\theta=1}^{n_\theta} \sum_{r=1}^{n_r} h_{\theta,r}^{(j)} h_{\theta,r}^{(k)} \cdot \text{Var}(p_\theta) \\ &\cong \sum_{\theta=1}^{n_\theta} \sum_{r=1}^{n_r} h_{\theta,r}^{(j)} h_{\theta,r}^{(k)} \cdot [A_{\theta,r}^2 N_{\theta,r}^2 W_r^2] p_{\theta,r} \end{aligned} \quad (\text{B.7})$$

where g_j and g_k are two pixel values of interest with reconstruction filters $h_{\theta,r}^{(j)}$ and $h_{\theta,r}^{(k)}$, respectively. The correlation coefficient of pixels g_j and g_k is given by

$$\begin{aligned} \rho(g_j, g_k) &= \frac{\text{Cov}(g_j, g_k)}{\sqrt{\text{Var}(g_j) \cdot \text{Var}(g_k)}} \\ &\cong \frac{\sum_{\theta=1}^{n_\theta} \sum_{r=1}^{n_r} h_{\theta,r}^{(j)} h_{\theta,r}^{(k)} \cdot [A_{\theta,r}^2 N_{\theta,r}^2 W_r^2] p_{\theta,r}}{\sqrt{\left\{ \sum_{\theta=1}^{n_\theta} \sum_{r=1}^{n_r} (h_{\theta,r}^{(j)})^2 [A_{\theta,r}^2 N_{\theta,r}^2 W_r^2] p_{\theta,r} \right\} \cdot \left\{ \sum_{\theta=1}^{n_\theta} \sum_{r=1}^{n_r} (h_{\theta,r}^{(k)})^2 [A_{\theta,r}^2 N_{\theta,r}^2 W_r^2] p_{\theta,r} \right\}}} \end{aligned} \quad (\text{B.8})$$

Assume that the pixel variances of g_j and g_k in an ROI are similar, and that the product $A_{\theta,r}^2 N_{\theta,r}^2 W_r^2 \cdot p_{\theta,r}$ is relatively uniform for those projection lines that substantially contribute to the sums, Eq. (B.8) can be further simplified as

$$\rho(g_j, g_k) \cong \frac{\sum_{\theta=1}^{n_\theta} \sum_{r=1}^{n_r} h_{\theta,r}^{(j)} h_{\theta,r}^{(k)}}{\sqrt{\left[\sum_{\theta=1}^{n_\theta} \sum_{r=1}^{n_r} (h_{\theta,r}^{(j)})^2 \right] \left[\sum_{\theta=1}^{n_\theta} \sum_{r=1}^{n_r} (h_{\theta,r}^{(k)})^2 \right]}}$$

$$\begin{aligned}
&= \frac{\sum_{\theta=1}^{n_\theta} \sum_{r=1}^{n_r} h_{\theta,r}^{(j)} h_{\theta,r}^{(k)}}{\sum_{\theta=1}^{n_\theta} \sum_{r=1}^{n_r} (h_{\theta,r})^2} \\
&= c_2 \cdot \sum_{\theta=1}^{n_\theta} \sum_{r=1}^{n_r} h_{\theta,r}^{(j)} h_{\theta,r}^{(k)} \tag{B.9}
\end{aligned}$$

where $c_2 \triangleq 1/(c_1 \cdot n_\theta)$. Thus, the correlation coefficient of any two pixels in an ROI is independent of the raw data and Eq. (B.9) can be used for a set of pixel pairs at various positions to produce a $\rho(d)$ table.

B.2 Covariance Computation in MAP images

The method used in this dissertation to compute the covariance of the MAP reconstruction image was originally developed by Fessler [19, 20]. Recently, Jinyi and Leahy [31] proposed a fast algorithm to reduce the computational complexity in Fessler's method. The following is a brief review of the fast covariance computation of MAP image described in [31].

B.2.1 MAP Reconstruction

A PET system can be modeled as independent Poisson random variables y with mean \bar{y} related to the emission intensity image x through an affine transform

$$\bar{y} = \mathbf{P}x + \mathbf{n} \tag{B.10}$$

where \mathbf{P} is the detection probability matrix and \mathbf{n} accounts for the presence of noise in the data. The detection probability matrix is modeled as $\mathbf{P} = D[n_i]\mathbf{G}$, where $D[n_i]$ is a diagonal matrix containing the correction factors, n_i , i.e. the product of the detector normalization, dead-time and attenuation correction factors¹. \mathbf{G} is the geometric projection matrix representing the probability that an emission from each voxel in the image produces, in the absence of attenuation effects, a photon pair at each of the detector pairs in the system. The log-likelihood function for the Poisson data model is

$$L(y|x) = \sum_i y_i \log \bar{y}_i - \bar{y}_i + \log y_i! \quad (\text{B.11})$$

The MAP reconstruction is usually described as the maximizer of the log posterior probability:

$$\hat{x}(y) = \arg \max_x L(y|x) - \beta U(x) \quad (\text{B.12})$$

where β is the hyper-parameter that determines the relative influence of the prior and likelihood terms, $L(y|x)$ is the log-likelihood function for the Poisson data model, and $U(x)$ is the Gibbs energy function depending on a sparse neighborhood matrix \mathbf{C} .

¹ $D[n_i]$ denotes a diagonal matrix with the (i, i) th diagonal element equal to n_i .

B.2.2 Approximation of Covariance

Based on a fixed point of the MAP objective function and using a truncated Taylor series expansion of the implicit estimator, Fessler [19, 20] developed a closed form for the computation of covariance in the MAP reconstruction image

$$\text{Cov}(\hat{x}) \cong [\mathbf{F} + \beta \mathbf{C}'\mathbf{C}]^{-1} \mathbf{F} [\mathbf{F} + \beta \mathbf{C}'\mathbf{C}]^{-1} \quad (\text{B.13})$$

where $\mathbf{F} = \mathbf{P}'D[1/\bar{y}_i]\mathbf{P}$ is the Fisher information matrix. This closed form involves a computation of the inverse of a Hessian matrix or solving a related set of linear equations. Hence, to reduce the computation complexity, Jinyi and Leahy [31] proposed a fast computation method which uses the following approximation for the Fisher information matrix

$$\mathbf{F} \cong \mathbf{D}_\kappa \mathbf{G}'\mathbf{G} \mathbf{D}_\kappa \quad (\text{B.14})$$

where $\mathbf{D}_\kappa = D[\kappa_j]$ with

$$\kappa_j \triangleq \sqrt{\frac{\sum_i g_{ij}^2 n_i^2 / \bar{y}_i}{\sum_i g_{ij}^2}}. \quad (\text{B.15})$$

Then,

$$\text{Cov}(\hat{x}) \cong \mathbf{D}_\kappa^{-1} \mathbf{B}(x)^{-1} \mathbf{G}'\mathbf{G} \mathbf{B}(x)^{-1} \mathbf{D}_\kappa^{-1} \quad (\text{B.16})$$

where

$$\mathbf{B}(x) \triangleq \mathbf{G}'\mathbf{G} + \beta\mathbf{D}_\kappa^{-1}\mathbf{C}'\mathbf{C}\mathbf{D}_\kappa^{-1}. \quad (\text{B.17})$$

The covariance can be further approximated using the following observations: (i) the matrix $\mathbf{B}(x)$ represents a local image blurring operator since the prior energy function is defined on a local neighborhood and the blurring function $\mathbf{G}'\mathbf{G}$ is also local; (ii) the correlation between voxels drops off rapidly as a function of the distance between them. The covariance with respect to voxel j is therefore dominated by the contribution of κ_j and the following approximation can be made:

$$\begin{aligned} \text{Cov}_j(\hat{x}) &\cong \mathbf{D}_\kappa^{-1}\mathbf{B}(x)^{-1}\mathbf{G}'\mathbf{G}\mathbf{B}(x)^{-1}\mathbf{D}_\kappa^{-1}\mathbf{e}_j \\ &\cong \kappa_j^{-2}\mathbf{K}(\beta\kappa_j^{-2})^{-1}\mathbf{G}'\mathbf{G}\mathbf{K}(\beta\kappa_j^{-2})^{-1}\mathbf{e}_j \end{aligned} \quad (\text{B.18})$$

where

$$\mathbf{K}(\beta\kappa_j^{-2}) = \mathbf{G}'\mathbf{G} + \beta\kappa_j^{-2}\mathbf{C}'\mathbf{C}. \quad (\text{B.19})$$

Since $\mathbf{G}'\mathbf{G}$ and $\mathbf{C}'\mathbf{C}$ correspond to the shift invariant blurring operators, they have a block Toeplitz structure and can be approximately diagonalized using the 2D discrete Fourier transform, i.e.,

$$\mathbf{G}'\mathbf{G} \cong \mathbf{Q}'\mathbf{D}[\lambda_i]\mathbf{Q}$$

$$\mathbf{C}'\mathbf{C} \cong \mathbf{Q}'D[\mu_i]\mathbf{Q} \quad (\text{B.20})$$

where \mathbf{Q} and \mathbf{Q}' , respectively, represent the Kronecker form of the 2D DFT matrix and its inverse, λ_i 's are the 2D Fourier transform of the system geometric response at the central voxel, and μ_i 's are the 2D Fourier transform of the central column of $\mathbf{C}'\mathbf{C}$. By Eq. (B.20), Eq. (B.19) can be written as

$$\mathbf{K}(\beta\kappa_j^{-2})^{-1} = \mathbf{Q}'D\left[\frac{1}{\lambda_i + \beta\kappa_j^{-2}\mu_i}\right]\mathbf{Q}. \quad (\text{B.21})$$

Then, the final covariance approximation formula becomes

$$\text{Cov}_j(\hat{x}) \cong \kappa_j^{-2}\mathbf{Q}'D\left[\frac{\lambda_i}{(\lambda_i + \beta\kappa_j^{-2}\mu_i)^2}\right]\mathbf{Q}\mathbf{e}_j. \quad (\text{B.22})$$

In cases where only a small ROI is considered, the correlation structure can be assumed to be invariant within the region. Hence the covariance matrix can be computed by one modified backprojection to compute the κ_j 's and one 2D FFT. One advantage of the above derivation is that λ_i and μ_i are independent of the data and can be pre-computed. Another advantage of Eq. (B.22) is that it is readily inverted which is an attractive property for the pre-whitening process of the non-white PET data for computer observer lesion detection.

Appendix C

GLRT Can Not Be Improved by Orthogonal Subspace Refining

Given two identified lesion subspace $\langle \mathbf{H} \rangle$ and normal tissue subspace $\langle \mathbf{S} \rangle$, the derived GLRT in chapter 5 can be written as

$$\begin{aligned} L_s(\mathbf{y}) &= \frac{\mathbf{y}^T \mathbf{P}_S^\perp \mathbf{y}}{\mathbf{y}^T \mathbf{P}_{HS}^\perp \mathbf{y}} \quad (\text{superimposed model}) \\ L_r(\mathbf{y}) &= \frac{\mathbf{y}^T \mathbf{P}_S^\perp \mathbf{y}}{\mathbf{y}^T \mathbf{P}_H^\perp \mathbf{y}} \quad (\text{replacement model}). \end{aligned} \quad (\text{C.1})$$

The refined subspace matrices by the orthogonal projection of $\langle \mathbf{H} \rangle$ onto the complement subspace of $\langle \mathbf{S} \rangle$ can be written as

$$\mathbf{S}' = \mathbf{S}, \quad \mathbf{H}' = \mathbf{P}_S^\perp \mathbf{H} \quad (\text{C.2})$$

where \mathbf{P}_S^\perp represents the orthogonal projection onto the complement subspace of $\langle \mathbf{S} \rangle$. Note that \mathbf{S}' is orthogonal to \mathbf{H}' . Then we have the following properties:

$$\mathbf{H}' = \mathbf{P}_S^\perp \mathbf{H} = \mathbf{H} - \mathbf{P}_S \mathbf{H} \implies \mathbf{P}_{H'} = \mathbf{P}_H - \mathbf{P}_{P_S \mathbf{H}} \quad (\text{C.3})$$

$$\mathbf{P}_{H'S'} = \mathbf{P}_{H'} + \mathbf{P}_{S'} = \mathbf{P}_{P_S^\perp \mathbf{H}} + \mathbf{P}_{S'} = \mathbf{P}_{P_S^\perp \mathbf{H}} + \mathbf{P}_S = \mathbf{P}_{HS}. \quad (\text{C.4})$$

Superimposed model

From the property in Eq. (C.4), the GLRT for superimposed model can be written as

$$L'_s(\mathbf{y}) = \frac{\mathbf{y}^T \mathbf{P}_{S'}^\perp \mathbf{y}}{\mathbf{y}^T \mathbf{P}_{H'S'}^\perp \mathbf{y}} = \frac{\mathbf{y}^T \mathbf{P}_S^\perp \mathbf{y}}{\mathbf{y}^T \mathbf{P}_{HS}^\perp \mathbf{y}} = L_s(\mathbf{y}) \quad (\text{C.5})$$

where the GLRTs before and after the orthogonal projection of the lesion subspace onto the orthogonal complement of the normal tissue subspace are shown to be equal.

Replacement model

The GLRT for the replacement model using \mathbf{H}' and \mathbf{S}' is

$$L'_r(\mathbf{y}) = \frac{\mathbf{y}^T \mathbf{P}_{S'}^\perp \mathbf{y}}{\mathbf{y}^T \mathbf{P}_{H'}^\perp \mathbf{y}}. \quad (\text{C.6})$$

Then, by using the property in Eq. (C.3), we have

$$\begin{aligned}
\frac{1}{L'_r(\mathbf{y})} &= \frac{\mathbf{y}^T \mathbf{P}_H^\perp \mathbf{y}}{\mathbf{y}^T \mathbf{P}_{S'}^\perp \mathbf{y}} \\
&= \frac{\mathbf{y}^T [\mathbf{P}_H^\perp + \mathbf{P}_{\mathbf{P}_S \mathbf{H}}] \mathbf{y}}{\mathbf{y}^T \mathbf{P}_{S'}^\perp \mathbf{y}} \\
&= \frac{1}{L_r(\mathbf{y})} + \frac{\mathbf{y}^T \mathbf{P}_{\mathbf{P}_S \mathbf{H}} \mathbf{y}}{\mathbf{y}^T \mathbf{P}_{S'}^\perp \mathbf{y}}.
\end{aligned} \tag{C.7}$$

Hence,

$$L'_r(\mathbf{y}) = \frac{1}{\frac{1}{L_r(\mathbf{y})} + \frac{\mathbf{y}^T \mathbf{P}_{\mathbf{P}_S \mathbf{H}} \mathbf{y}}{\mathbf{y}^T \mathbf{P}_{S'}^\perp \mathbf{y}}} < L_r(\mathbf{y}). \tag{C.8}$$

Eq. (C.8) shows that, for the replacement model, the performance of the GLRT after applying the orthogonal projection refined subspaces is inferior to that using the original subspaces, because the scalar, $\frac{\mathbf{y}^T \mathbf{P}_{\mathbf{P}_S \mathbf{H}} \mathbf{y}}{\mathbf{y}^T \mathbf{P}_{S'}^\perp \mathbf{y}}$, is positive.

Appendix D

Multi-Pixel GLRT Derivation

Given an ROI with P number of pixels, let the P -dimensional column vector $\mathbf{f}_i \triangleq [f_i(1), f_i(2), \dots, f_i(P)]^T$ denote the spatial pixel data for the i -th frame and let the ROI data $\mathbf{F}_{P \times N} = [\mathbf{f}_1, \mathbf{f}_2, \dots, \mathbf{f}_N]$. We assume that all the columns of the matrix \mathbf{F} are independent. Let $\mathbf{Y}_{N \times P} \triangleq [\mathbf{y}_1, \mathbf{y}_2, \dots, \mathbf{y}_P] = \mathbf{F}^T$.

The hypothesis data model for the ROI under the replacement model assumption is

$$\begin{cases} H_0 : \mathbf{Y} = \mathbf{X}_0 + \mathbf{N}_0 \\ H_1 : \mathbf{Y} = \mathbf{X}_1 + \mathbf{N}_1 \end{cases} \quad (\text{D.1})$$

where the noise \mathbf{N}_i is assumed to be a multivariate normal (MVN) with zero mean.

It is also assumed that the signal \mathbf{X}_i obeys the linear subspace model, i.e.,

$$\begin{aligned} \mathbf{X}_0 &= \mathbf{S}\Phi_0 \\ \mathbf{X}_1 &= \mathbf{H}\Phi_1 \end{aligned} \quad (\text{D.2})$$

where \mathbf{H} and \mathbf{S} are the lesion and normal tissue subspaces, respectively, and Φ_i is the corresponding coefficient matrix. Hence, the mean of temporal-spatial ROI data becomes

$$\mathbf{E}\{\mathbf{Y}\} = \begin{cases} \mathbf{S}\Phi_0, & \text{under hypothesis } H_0 \\ \mathbf{H}\Phi_1, & \text{under hypothesis } H_1. \end{cases} \quad (\text{D.3})$$

We assume that the spatial covariance matrix for each frame has the same structure but with different energy level [7]. That means the spatial covariance matrix for the i -th frame can be written as $\sigma_i \mathbf{M}$, i.e.,

$$\text{cov}(\mathbf{f}_i) = \sigma_i \mathbf{M}, \quad i = 1, \dots, N \quad (\text{D.4})$$

where \mathbf{M} is the spatial inter-pixel correlation matrix for all frames. Let $\mathbf{Z} = \mathbf{M}^{-1/2} \mathbf{F}$, then the *variance* matrix for the whitened data \mathbf{Z} is

$$\text{var}(\mathbf{Z}) = \begin{bmatrix} \sigma_1 & \sigma_2 & \cdots & \sigma_N \\ \sigma_1 & \sigma_2 & \cdots & \sigma_N \\ \vdots & \vdots & \ddots & \vdots \\ \sigma_1 & \sigma_2 & \cdots & \sigma_N \end{bmatrix}_{P \times N}. \quad (\text{D.5})$$

Let $\mathbf{R} \triangleq [\mathbf{r}_1, \mathbf{r}_2, \dots, \mathbf{r}_P] = \mathbf{Z}^T$. Then the covariance matrix for *each* column of \mathbf{R} is

$$\text{cov}(\mathbf{r}_i) = \begin{bmatrix} \sigma_1 & 0 & \cdots & 0 \\ 0 & \sigma_2 & \cdots & 0 \\ \vdots & \vdots & \ddots & \vdots \\ 0 & 0 & \cdots & \sigma_N \end{bmatrix}_{N \times N} \triangleq \mathbf{\Lambda}, \quad i = 1, 2, \dots, P. \quad (\text{D.6})$$

The ROI data will be statistically described as a Gaussian probability density function (PDF) based on the temporal-spatial data matrix \mathbf{R} . After the whitening process, by the independence of the columns \mathbf{r}_i in \mathbf{R} , the joint Gaussian PDF of \mathbf{R} under hypothesis, say H_1 , becomes

$$\begin{aligned}
& f_1(\mathbf{R}) \\
&= f(\mathbf{r}_1, \mathbf{r}_2, \dots, \mathbf{r}_P | H_1) \\
&= \prod_{i=1}^P f(\mathbf{r}_i | H_1) \\
&= \prod_{i=1}^P (2\pi)^{-N/2} |\mathbf{\Lambda}_1|^{-1/2} \exp \left\{ \frac{-1}{2} [\mathbf{r}_i - \mathbf{E}(\mathbf{r}_i)]^T \mathbf{\Lambda}_1^{-1} [\mathbf{r}_i - \mathbf{E}(\mathbf{r}_i)] \right\} \\
&= (2\pi)^{-NP/2} |\mathbf{\Lambda}_1|^{-P/2} \exp \left\{ \frac{-1}{2} \sum_{i=1}^P [\mathbf{r}_i - \mathbf{E}(\mathbf{r}_i)]^T \mathbf{\Lambda}_1^{-1} [\mathbf{r}_i - \mathbf{E}(\mathbf{r}_i)] \right\} \\
&= (2\pi)^{-NP/2} |\mathbf{\Lambda}_1|^{-P/2} \text{etr} \left\{ \frac{-1}{2} [\mathbf{R} - \mathbf{E}(\mathbf{R})]^T \mathbf{\Lambda}_1^{-1} [\mathbf{R} - \mathbf{E}(\mathbf{R})] \right\} \\
&= (2\pi)^{-NP/2} |\mathbf{\Lambda}_1|^{-P/2} \text{etr} \left\{ \frac{-1}{2} \mathbf{\Lambda}_1^{-1} [\mathbf{R} - \mathbf{E}(\mathbf{R})] [\mathbf{R} - \mathbf{E}(\mathbf{R})]^T \right\} \tag{D.7}
\end{aligned}$$

where “etr” denotes “exp trace”, and

$$\begin{aligned}
\mathbf{E}(\mathbf{R}) &= \mathbf{E}(\mathbf{Z}^T) = \mathbf{E} \left([\mathbf{M}^{-1/2} \mathbf{F}]^T \right) = \mathbf{E}(\mathbf{F}^T \mathbf{M}^{-1/2}) \\
&= \mathbf{E}(\mathbf{Y}) \mathbf{M}^{-1/2} = \mathbf{H} \mathbf{\Phi}_1 \mathbf{M}^{-1/2}. \tag{D.8}
\end{aligned}$$

If we further assume that the mean of image is the same for all frame, i.e.,

$$\Phi_1 \triangleq \phi_1 \mathbf{1}^T \quad (\text{D.9})$$

where ϕ_1 is the coefficient vector for all frames and $\mathbf{1}^T = [1, 1, \dots, 1]$. Then,

$$\begin{aligned} \mathbf{E}(\mathbf{R}) &= \mathbf{H}\phi_1 \mathbf{1}^T \mathbf{M}^{-1/2} \\ &\triangleq \mathbf{b}_1 \mathbf{s}^T \end{aligned} \quad (\text{D.10})$$

where $\mathbf{b}_1 \triangleq \mathbf{H}\phi_1$ and $\mathbf{s}^T \triangleq \mathbf{1}^T \mathbf{M}^{-1/2}$. Hence, the PDF for \mathbf{R} becomes

$$f(\mathbf{R}) = (2\pi)^{-NP/2} |\Lambda_1|^{-P/2} \text{etr} \left\{ \frac{-1}{2} \Lambda_1^{-1} (\mathbf{R} - \mathbf{b}_1 \mathbf{s}^T) (\mathbf{R} - \mathbf{b}_1 \mathbf{s}^T)^T \right\}. \quad (\text{D.11})$$

In order to apply the generalized likelihood ratio test (GLRT) for the matched subspace detector, the next step is to find the maximum likelihood estimate (MLE) of Λ_1 and ϕ_1 . Based on (D.11), the MLE of Λ_1 can be simply written as

$$\hat{\Lambda}_1 = \frac{1}{P} (\mathbf{R} - \mathbf{b}_1 \mathbf{s}^T) (\mathbf{R} - \mathbf{b}_1 \mathbf{s}^T)^T. \quad (\text{D.12})$$

The MLE of ϕ_1 can be derived from the minimization of $|\mathbf{F}_{\mathbf{b}_1}|$, i.e.,

$$L(\mathbf{R}) = \min_{\mathbf{b}_1} |\mathbf{F}_{\mathbf{b}_1}| \quad (\text{D.13})$$

where

$$\mathbf{F}_{\mathbf{b}_1} \triangleq (\mathbf{R} - \mathbf{b}_1 \mathbf{s}^T)(\mathbf{R} - \mathbf{b}_1 \mathbf{s}^T)^T. \quad (\text{D.14})$$

Now expand $\mathbf{F}_{\mathbf{b}_1}$ as follows:

$$\mathbf{F}_{\mathbf{b}_1} = \mathbf{R}\mathbf{R}^T - \mathbf{R}\mathbf{s}\mathbf{b}_1^T - \mathbf{b}_1\mathbf{s}^T\mathbf{R}^T + \mathbf{b}_1\mathbf{s}^T\mathbf{s}\mathbf{b}_1^T. \quad (\text{D.15})$$

Let $\tilde{\mathbf{s}} \triangleq (\mathbf{s}^T\mathbf{s})^{1/2}\mathbf{s}$ and $\tilde{\mathbf{b}}_1 \triangleq (\mathbf{s}^T\mathbf{s})^{1/2}\mathbf{b}_1$, so $\tilde{\mathbf{b}}_1\tilde{\mathbf{s}}^T = \mathbf{b}_1\mathbf{s}^T$. After the change of variables,

$$\begin{aligned} \mathbf{F}_{\tilde{\mathbf{b}}_1} &= \mathbf{R}\mathbf{R}^T - \mathbf{R}\tilde{\mathbf{s}}\tilde{\mathbf{b}}_1^T - \tilde{\mathbf{b}}_1\tilde{\mathbf{s}}^T\mathbf{R}^T + \tilde{\mathbf{b}}_1\tilde{\mathbf{b}}_1^T \\ &= (\tilde{\mathbf{b}}_1 - \mathbf{R}\tilde{\mathbf{s}})(\tilde{\mathbf{b}}_1 - \mathbf{R}\tilde{\mathbf{s}})^T + \mathbf{R}\mathbf{R}^T - (\mathbf{R}\tilde{\mathbf{s}})(\mathbf{R}\tilde{\mathbf{s}})^T \\ &= (\tilde{\mathbf{b}}_1 - \mathbf{R}\tilde{\mathbf{s}})(\tilde{\mathbf{b}}_1 - \mathbf{R}\tilde{\mathbf{s}})^T + \mathbf{G} \end{aligned} \quad (\text{D.16})$$

where $\mathbf{G} \triangleq \mathbf{R}\mathbf{R}^T - (\mathbf{R}\tilde{\mathbf{s}})(\mathbf{R}\tilde{\mathbf{s}})^T$ and \mathbf{G} can be shown to be invertible [52]. Hence,

$$\begin{aligned} |\mathbf{F}_{\tilde{\mathbf{b}}_1}| &= |\mathbf{G}| \cdot |\mathbf{I} + (\tilde{\mathbf{b}}_1 - \mathbf{R}\tilde{\mathbf{s}})(\tilde{\mathbf{b}}_1 - \mathbf{R}\tilde{\mathbf{s}})^T\mathbf{G}^{-1}| \\ &= |\mathbf{G}| \cdot |\mathbf{I} + \mathbf{a}\mathbf{a}^T\mathbf{G}^{-1}| \end{aligned} \quad (\text{D.17})$$

where $\mathbf{a} \triangleq \tilde{\mathbf{b}}_1 - \mathbf{R}\tilde{\mathbf{s}}$. Now multiply the matrix $\mathbf{D} \triangleq \mathbf{I} + \mathbf{a}\mathbf{a}^T\mathbf{G}^{-1}$ by \mathbf{a} as follows:

$$\mathbf{D}\mathbf{a} = \mathbf{a} + \mathbf{a}(\mathbf{a}^T\mathbf{G}^{-1}\mathbf{a})$$

$$= (1 + \mathbf{a}^T \mathbf{G}^{-1} \mathbf{a}) \mathbf{a} \quad (\text{D.18})$$

which shows that \mathbf{a} is an eigenvector of \mathbf{D} with the associated eigenvalue $1 + \mathbf{a}^T \mathbf{G}^{-1} \mathbf{a}$.

Let \mathbf{v}_i , for $i = 1, 2, \dots, N - 1$, be some orthogonal set of vectors, all perpendicular to the vector $\mathbf{G}^{-1} \mathbf{a}$. Then,

$$\begin{aligned} \mathbf{D} \mathbf{v}_i &= (\mathbf{I} + \mathbf{a} \mathbf{a}^T \mathbf{G}^{-1}) \mathbf{v}_i \\ &= \mathbf{v}_i + \mathbf{a} [(\mathbf{G}^{-1} \mathbf{a})^T \mathbf{v}_i] \\ &= \mathbf{v}_i \end{aligned} \quad (\text{D.19})$$

which means \mathbf{v}_i is an eigenvector of \mathbf{D} with eigenvalue equal to one, for $i = 1, 2, \dots, N - 1$.

1. So Eq. (D.16) becomes

$$\begin{aligned} |\mathbf{F}_{\tilde{\mathbf{b}}_1}| &= |\mathbf{G}| \cdot (1 + \mathbf{a}^T \mathbf{G}^{-1} \mathbf{a}) \\ &= |\mathbf{G}| \cdot [1 + (\tilde{\mathbf{b}}_1 - \mathbf{R} \tilde{\mathbf{s}})^T \mathbf{G}^{-1} (\tilde{\mathbf{b}}_1 - \mathbf{R} \tilde{\mathbf{s}})] \\ &= |\mathbf{G}| \cdot [1 + (\tilde{\mathbf{H}} \phi_1 - \mathbf{R} \tilde{\mathbf{s}})^T \mathbf{G}^{-1} (\tilde{\mathbf{H}} \phi_1 - \mathbf{R} \tilde{\mathbf{s}})] \end{aligned} \quad (\text{D.20})$$

where $\tilde{\mathbf{H}} \triangleq (\mathbf{s}^T \mathbf{s})^{1/2} \mathbf{H}$. The minimum of $|\mathbf{F}_{\tilde{\mathbf{b}}_1}|$ can be derived by using

$$\frac{\partial}{\partial \phi_1} \mathbf{m}^T \mathbf{Q} \mathbf{m} = 2 \left(\frac{\partial}{\partial \phi_1} \mathbf{m}^T \right) \mathbf{Q} \mathbf{m} \quad (\text{D.21})$$

provided \mathbf{Q} is independent of ϕ_1 . Then we have

$$\phi_{1,min} = (\tilde{\mathbf{H}}^T \mathbf{G}^{-1} \tilde{\mathbf{H}})^{-1} \tilde{\mathbf{H}}^T \mathbf{G}^{-1} \mathbf{R} \tilde{\mathbf{s}}. \quad (\text{D.22})$$

Hence,

$$\begin{aligned} & |\mathbf{F} \phi_1|_{min} \\ = & |\mathbf{G}| \cdot \left\{ 1 + \left[\tilde{\mathbf{H}} (\tilde{\mathbf{H}}^T \mathbf{G}^{-1} \tilde{\mathbf{H}})^{-1} \tilde{\mathbf{H}}^T \mathbf{G}^{-1} \mathbf{R} \tilde{\mathbf{s}} - \mathbf{R} \tilde{\mathbf{s}} \right]^T \mathbf{G}^{-1} \right. \\ & \left. \cdot \left[\tilde{\mathbf{H}} (\tilde{\mathbf{H}}^T \mathbf{G}^{-1} \tilde{\mathbf{H}})^{-1} \tilde{\mathbf{H}}^T \mathbf{G}^{-1} \mathbf{R} \tilde{\mathbf{s}} - \mathbf{R} \tilde{\mathbf{s}} \right] \right\} \\ = & |\mathbf{G}| \cdot \left\{ 1 + \left[\mathbf{G}^{-1/2} \tilde{\mathbf{H}} (\tilde{\mathbf{H}}^T \mathbf{G}^{-1} \tilde{\mathbf{H}})^{-1} \tilde{\mathbf{H}}^T \mathbf{G}^{-1/2} \mathbf{G}^{-1/2} \mathbf{R} \tilde{\mathbf{s}} - \mathbf{G}^{-1/2} \mathbf{R} \tilde{\mathbf{s}} \right]^T \right. \\ & \left. \cdot \left[\mathbf{G}^{-1/2} \tilde{\mathbf{H}} (\tilde{\mathbf{H}}^T \mathbf{G}^{-1} \tilde{\mathbf{H}})^{-1} \tilde{\mathbf{H}}^T \mathbf{G}^{-1/2} \mathbf{G}^{-1/2} \mathbf{R} \tilde{\mathbf{s}} - \mathbf{G}^{-1/2} \mathbf{R} \tilde{\mathbf{s}} \right] \right\} \\ = & |\mathbf{G}| \cdot \left\{ 1 + \left[\bar{\mathbf{H}} (\bar{\mathbf{H}}^T \bar{\mathbf{H}})^{-1} \bar{\mathbf{H}}^T \mathbf{G}^{-1/2} \mathbf{R} \tilde{\mathbf{s}} - \mathbf{G}^{-1/2} \mathbf{R} \tilde{\mathbf{s}} \right]^T \right. \\ & \left. \cdot \left[\bar{\mathbf{H}} (\bar{\mathbf{H}}^T \bar{\mathbf{H}})^{-1} \bar{\mathbf{H}}^T \mathbf{G}^{-1/2} \mathbf{R} \tilde{\mathbf{s}} - \mathbf{G}^{-1/2} \mathbf{R} \tilde{\mathbf{s}} \right] \right\} \\ & \text{where } \bar{\mathbf{H}} \triangleq \mathbf{G}^{-1/2} \tilde{\mathbf{H}} \\ = & |\mathbf{G}| \cdot \left\{ 1 + \left[(\mathbf{P}_{\bar{\mathbf{H}}} - \mathbf{I}) \mathbf{G}^{-1/2} \mathbf{R} \tilde{\mathbf{s}} \right]^T \left[(\mathbf{P}_{\bar{\mathbf{H}}} - \mathbf{I}) \mathbf{G}^{-1/2} \mathbf{R} \tilde{\mathbf{s}} \right] \right\} \\ = & |\mathbf{G}| \cdot \left\{ 1 + \left[\mathbf{G}^{-1/2} \mathbf{R} \tilde{\mathbf{s}} \right]^T \mathbf{P}_{\bar{\mathbf{H}}}^\perp \left[\mathbf{G}^{-1/2} \mathbf{R} \tilde{\mathbf{s}} \right] \right\} \quad (\text{D.23}) \end{aligned}$$

where $\mathbf{P}_{\bar{\mathbf{H}}}$ is an orthogonal projection matrix onto the subspace of $\bar{\mathbf{H}}$, and $\mathbf{P}_{\bar{\mathbf{H}}}^\perp$ is an orthogonal projection matrix onto the complement subspace of $\bar{\mathbf{H}}$.

Now, the GLRT for the ROI data matrix can be derived easily. Based on the assumptions made for the ROI data model in this Appendix, the detection problem becomes a test of the distributions:

$$\begin{cases} H_0 & : \mathbf{Y} : N[\mathbf{S}\phi_0\mathbf{1}^T, \mathbf{\Lambda}_0 \otimes \mathbf{M}] \\ H_1 & : \mathbf{Y} : N[\mathbf{H}\phi_1\mathbf{1}^T, \mathbf{\Lambda}_1 \otimes \mathbf{M}] \end{cases} \quad (\text{D.24})$$

which is equivalent to

$$\begin{cases} H_0 & : \mathbf{R} \triangleq \mathbf{Y}\mathbf{M}^{-1/2} : N[\mathbf{S}\phi_0\mathbf{1}^T\mathbf{M}^{-1/2}, \mathbf{\Lambda}_0 \otimes \mathbf{I}] \\ H_1 & : \mathbf{R} \triangleq \mathbf{Y}\mathbf{M}^{-1/2} : N[\mathbf{H}\phi_1\mathbf{1}^T\mathbf{M}^{-1/2}, \mathbf{\Lambda}_1 \otimes \mathbf{I}] \end{cases} \quad (\text{D.25})$$

where \otimes denotes the Kronecker product. The likelihood ratio test can be written as

$$l(\mathbf{Y}) = \frac{L(\phi_1, \mathbf{\Lambda}_1; \mathbf{Y})}{L(\phi_0, \mathbf{\Lambda}_0; \mathbf{Y})} = \frac{L(\mathbf{b}_1, \mathbf{\Lambda}_1; \mathbf{R})}{L(\mathbf{b}_0, \mathbf{\Lambda}_0; \mathbf{R})}. \quad (\text{D.26})$$

Hence, the GLRT can be derived by substituting the MLE of $\mathbf{\Lambda}_i$ and Φ_i :

$$\hat{l}(\mathbf{Y}) = \frac{L(\hat{\mathbf{b}}_1, \hat{\mathbf{\Lambda}}_1; \mathbf{R})}{L(\hat{\mathbf{b}}_0, \hat{\mathbf{\Lambda}}_0; \mathbf{R})} = \left(\frac{|\hat{\mathbf{\Lambda}}_0|}{|\hat{\mathbf{\Lambda}}_1|} \right)^{P/2}. \quad (\text{D.27})$$

Then it is more convenient to replace the GLRT by the $(P/2)$ -root GLRT

$$\begin{aligned} l_2(\mathbf{Y}) &= [\hat{l}(\mathbf{Y})]^{2/P} = \frac{|\hat{\mathbf{\Lambda}}_0|}{|\hat{\mathbf{\Lambda}}_1|} \\ &= \frac{|\mathbf{G}| \cdot \left\{ 1 + (\mathbf{G}^{-1/2}\mathbf{R}\tilde{\mathbf{s}})^T \mathbf{P}_{\tilde{\mathbf{S}}}^\perp (\mathbf{G}^{-1/2}\mathbf{R}\tilde{\mathbf{s}}) \right\}}{|\mathbf{G}| \cdot \left\{ 1 + (\mathbf{G}^{-1/2}\mathbf{R}\tilde{\mathbf{s}})^T \mathbf{P}_{\tilde{\mathbf{H}}}^\perp (\mathbf{G}^{-1/2}\mathbf{R}\tilde{\mathbf{s}}) \right\}} \\ &= \frac{1 + (\mathbf{G}^{-1/2}\mathbf{R}\tilde{\mathbf{s}})^T \mathbf{P}_{\tilde{\mathbf{S}}}^\perp (\mathbf{G}^{-1/2}\mathbf{R}\tilde{\mathbf{s}})}{1 + (\mathbf{G}^{-1/2}\mathbf{R}\tilde{\mathbf{s}})^T \mathbf{P}_{\tilde{\mathbf{H}}}^\perp (\mathbf{G}^{-1/2}\mathbf{R}\tilde{\mathbf{s}})}. \end{aligned} \quad (\text{D.28})$$

**Appendix B: Presentation at SNM Annual Conference,
Torrance, Ca. June 2001**

Assessment of ROI-based Time Activity Analyses in Dynamic PET for Oncology

X. Yu, C.C. Huang and P. S. Conti

PET Imaging Science Center, USC



OBJECTIVE

- To develop a method for detecting tumors in PET images based on
 - time activity curve (TAC) information
- To perform an assessment on three TAC evaluation methods for tumor detection with
 - receiver operating characteristic (ROC) study

APPROACH

- 1) Implement three TAC evaluation methods in computer software
- 2) Build a machine observer with three different TAC evaluations
- 3) Generate phantom dynamic raw data with or without artificial lesions and reconstruct FBP images from the raw data
- 4) Use machine observer to evaluate the phantom images and perform ROC study

TAC EVALUATION METHOD 1

- Assuming no spatial correlation between pixels
 - Averaging TACs over ROI
 - Averaging operation will lower the noise to certain extent if no inter-pixel correlation

TAC EVALUATION METHOD 2

- Assuming inter-pixel correlation
 - Compute ROI covariance matrix frame by frame
 - Averaging TACs over ROI after inter-pixel decorrelation

TAC EVALUATION METHOD 3

- Assuming that each frame has the same inter-pixel correlation structure R , but with different energy levels: $R_i = \sigma_i R$
 - Compute ROI covariance matrix from the least noisy frame
 - Decorrelate ROI with the covariance
 - Averaging TACs over ROI after inter-pixel decorrelation

COVARIANCE MATRIX COMPUTATION

- **Huesman's analytical computation:**
 - based on uncorrelation of PET projection data and linearity of FBP
- **Carson's simplification formulae:**
 - assume that the statistics of neighboring projections are similar
 - covariance is independent of raw data

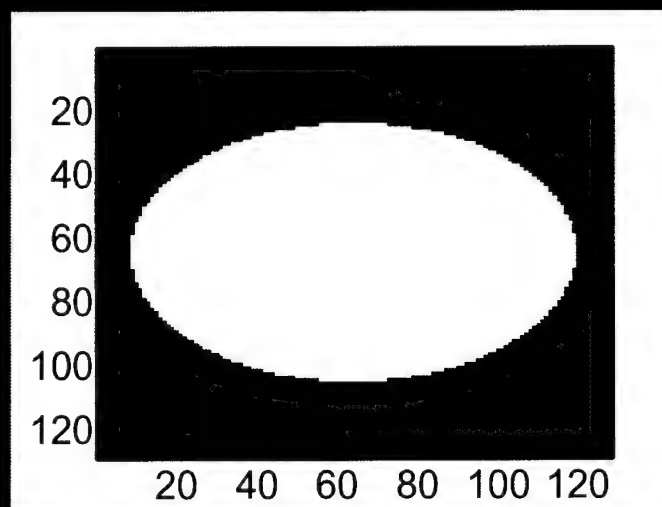
MACHINE OBSERVER

- **Design principle: the maximum likelihood ratio test**
- **Function: For a given ROI, make a decision based on the likelihood that the observed TACs are in**
 - a lesion or
 - normal tissues

DATA FOR STUDAY

- Computer generated phantom dynamic data
 - Each data sequence was set to contain 5 artificial lesions or no lesions
 - 50 sets in total are generated for each setting

PHANTOM



PHANTOM: FBP

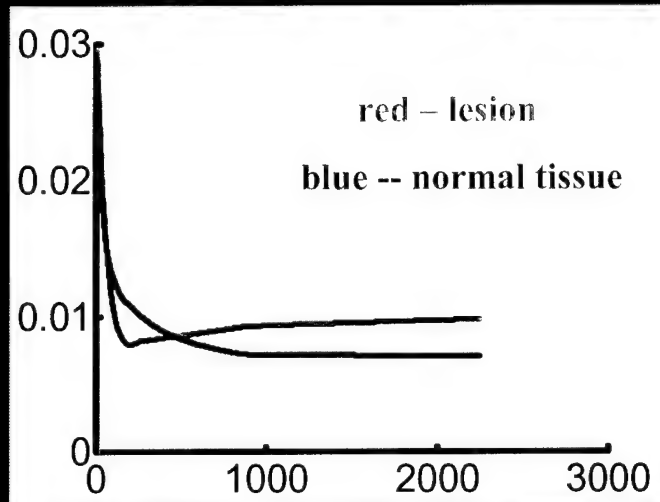
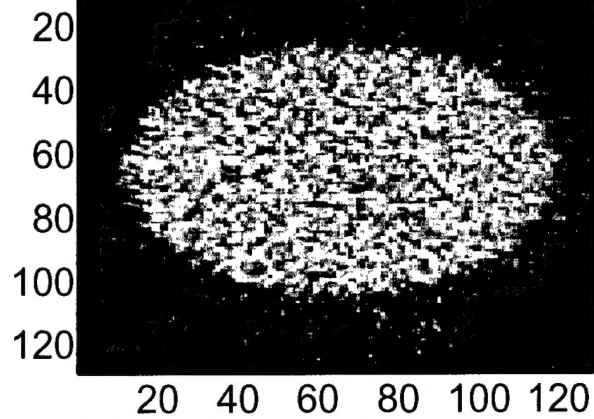


IMAGE GENERATION AND RECONSTRUCTION

- Forward projection with
 - system blurring
 - Poisson noise generation
- Filtered backprojection (FBP) with
 - Han filter and 0.5 cutting frequency

PHANTOM: FBP



NOTATION

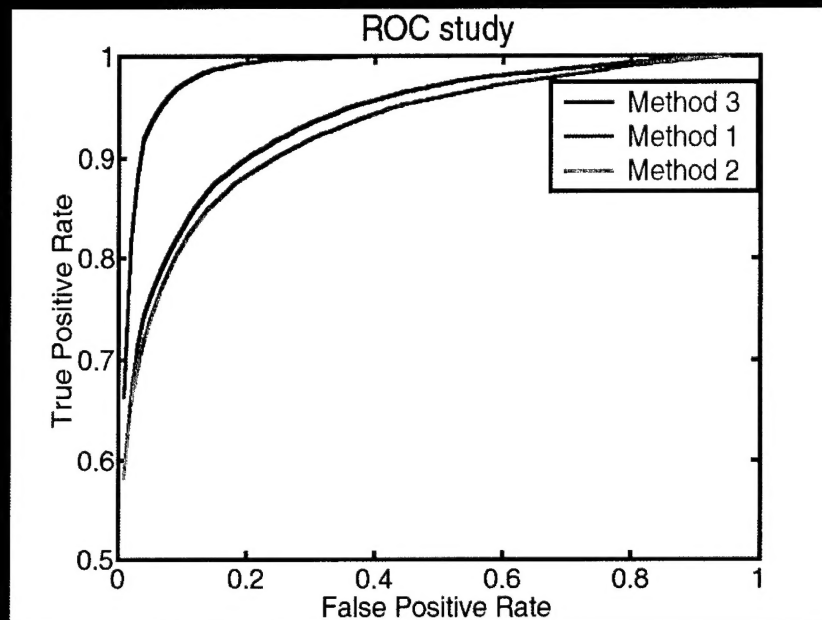
- **TP:** True Positive
- **TN:** True Negative
- **FP:** False Positive
- **FN:** False Negative
- **PPV:** Positive Predication Value
- **NPV:** Negative Predication Value

DEFINITIONS

- **Accuracy:** $(TP+TN)/(TP+TN+FP+FN)$
- **Sensitivity:** $TP/(TP+FN)$
- **Specificity:** $TN/(TN+FP)$
- **PPV:** $TP/(TP+FP)$
- **NPV:** $TN/(TN+FN)$
- **Az:** Area under curve

ROC PERFORMANCE

	Method 1	Method 2	Method 3
Accuracy	0.79	0.77	0.88
Sensitivity	0.77	0.77	0.79
Specificity	0.81	0.77	0.97
PPV	0.80	0.77	0.96
NPV	0.81	0.77	0.97
Az	0.93	0.92	0.98



RESULTS AND COMPARISON

- Compared to Methods 1 and 2, Method 3 increased:
 - Specificity by 20%
 - Accuracy by 11%
 - Area under curve by 6.5%

CONCLUSION

- **No significant difference between Methods 1 and 2, possibly due to**
 - **inaccurate covariance matrix estimation in the early noisy frames**
 - **simplified covariance matrix computation**
- **Constrained inter-pixel decorrelation improves TAC-based lesion detection**